

ARPE - final report

Search for excited Ξ_{cc}^{++} baryons at
the LHCb experiment

Paul GAIGNE

supervised by Marco Pappagallo



Contents

1	Introduction	1
2	Analysis strategy	2
3	Data	4
3.1	Data	4
3.1.1	$\Xi_{cc}^{++} \rightarrow \Lambda_c^+ K^- \pi^+ \pi^+$ exclusive line	4
3.1.2	$\Lambda_c^+ \rightarrow p^+ K^- \pi^+$ inclusive line	4
4	$\Xi_{cc}^{++} \rightarrow \Lambda_c^+ K^- \pi^+ \pi^+$ exclusive trigger line	5
4.1	Simulation	5
4.1.1	MC truth matching	5
4.2	Selection	6
4.2.1	Trigger requirements	6
4.2.2	Offline reconstruction and pre-selection	8
4.2.3	Multivariate selection	8
4.2.4	Measurement of the Ξ_{cc}^{++} mass	14
5	$\Xi_{cc}^{++} \rightarrow \Lambda_c^+ K^- \pi^+ \pi^+$ inclusive line	16
5.1	Simulation	16
5.1.1	MC truth matching	16
5.2	Selection	16
5.2.1	Trigger requirements	17
5.2.2	Offline reconstruction and pre-selection	19
5.2.3	Multivariate selection	20
5.2.4	Removal of internal track clone candidates and duplicated candidates	23
5.3	Significance optimization and mass fit	24
6	Search for excited doubly charmed baryons	27
6.1	Strategy	27
6.2	MC simulation	27
6.2.1	MC truth matching	27
6.3	Selection	29
6.3.1	Offline reconstruction and pre-selection	29
6.3.2	Multivariate selection	29
6.3.3	Removal of internal track clone candidates and duplicated candidates	37
6.4	Mass fit	37
6.4.1	MC mass fit	38
6.4.2	Background fit	39
6.5	Mass distributions and signal significance	39
7	Conclusion	42
Appendices		43

A	Introduction of the detector	43
A.1	Sub-detectors	43
A.2	Trigger levels	44
A.3	Dataflow	45
B	Sanity checks	46
B.1	Polarity	46
B.2	Charge conjugations	46
B.3	Λ_c^+ signal vs sidebands	47
C	MVA training results with Ξ_{cc}^{++} Tight selection	48
	References	54

1 Introduction

The quark model [1–3] predicts the existence of multiplets of baryon and meson states, with a structure determined by the symmetry properties of the hadron wavefunctions. When the first four flavours of quarks (u , d , s , and c) are considered, the states form SU(4) multiplets [4]. All the ground states with the charm quantum number $C = 0$ or $C = 1$ have been discovered [5]. Three weakly decaying $C = 2$ states are expected: a Ξ_{cc} isodoublet (ccu , ccd) and an Ω_{cc}^+ isosinglet (ccs), each with spin-parity quantum numbers $J^P = 1/2^+$ (see Fig. 1a). Such states provide an unique system for testing models of quantum chromodynamics (QCD), the theory which describes the strong interaction. Before 2017, none of these doubly charmed baryons had unambiguous experimental evidence. A lot of theoretical models have calculated the properties of these states. According to the isospin symmetry between the u and the d quarks, the Ξ_{cc}^+ mass should be very similar to that of the Ξ_{cc}^{++} baryon. For most theoretical models the predicted Ξ_{cc} mass ranges between 3500 and 3700 MeV/ c^2 [6–12].

In 2017, a study performed by the LHCb collaboration reported the observation of $\Xi_{cc}^{++} \rightarrow \Lambda_c^+ K^- \pi^+ \pi^+$, and the mass was measure to be 3621.40 ± 0.72 (stat) ± 0.27 (syst) ± 0.14 (Λ_c^+) MeV/ c^2 [13]. This was followed by the first measurement of the lifetime $\tau(\Xi_{cc}^{++}) = 0.256 \pm 0.024$ (stat) ± 0.014 (syst) ps performed using the same decay mode [14]. In 2018, LHCb also reported the first observation of $\Xi_{cc}^{++} \rightarrow \Xi_c^+ \pi^+$, with the measured mass 3620.6 ± 1.5 (stat) \pm (syst) $\pm (\Lambda_c^+)$ MeV/ c^2 [15]. Both decay modes are firstly observed with 2016 data collected by LHCb, at a center-of-mass energy of 13 TeV and corresponding to an integrated luminosity of 1.7 fb^{-1} . In 2019, a new study updated the mass measurement using both decay mode with the full Run 2 data collected by LHCb [16]. Finally in 2021, a study reported the first observation of $\Xi_{cc}^{++} \rightarrow \Xi_c'^+ \pi^+$ [17].

After 2017, studies have been made for the other doubly charmed baryons. In 2019, a new study [18] performed by LHCb search for the $\Xi_{cc}^+ \rightarrow \Lambda_c^+ K^- \pi^+$ decay after the previous ones made by SELEX in 2002 [19] and LHCb in 2013 [20]. In 2021, LHCb also studied the $\Xi_{cc}^{++} \rightarrow \Xi_c^+ \pi^- \pi^+$ decay [21] and LHCb performed their first search for the last doubly charmed baryons Ω_{cc}^+ in final state $\Xi_c^+ K^- \pi^+$ [22]. No significant signal has been observed by these analyses and the Ξ_{cc}^{++} remains the only known doubly charmed baryon.

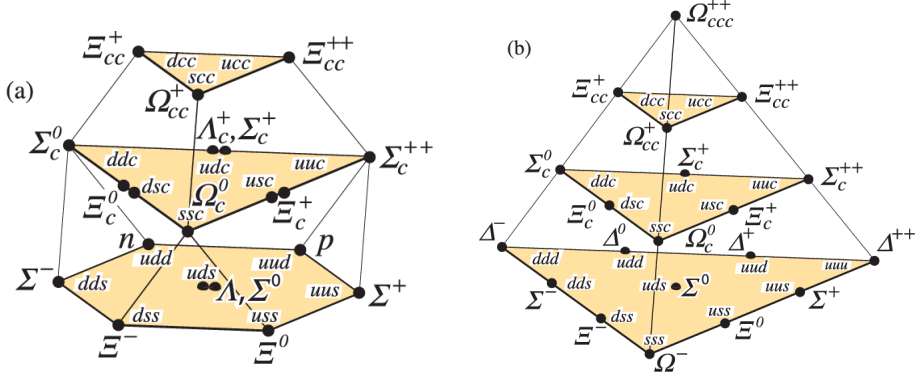


Figure 1: SU(4) multiplets of qqq baryons made of u , d , s , and c quarks: (a) the 20 multiplet with $J^P = 1/2^+$ containing the baryon octet, and (b) the 20 multiplet with $J^P = 3/2^+$ containing the baryon decuplet.

My research focuses on the search of excited states of unobserved doubly charmed baryons with a spin parity $J^P = 3/2^+$ (see Fig. 1b). Figure 2 shows an example of the possible Feynman diagrams of the two decays $\Xi_{cc}^{***} \rightarrow \Xi_{cc}^{++}\pi^-$ and $\Omega_{cc}^{***} \rightarrow \Xi_{cc}^{++}K^-$ studied.

The origin of Ξ_{cc}^{++} candidates have been quantified in [23], the result using a quark-diquark production model are $\sim 30\%$ from $\Xi_{cc}^{***+} \rightarrow \Xi_{cc}^{++}\pi^0$, $\sim 15\%$ from $\Xi_{cc}^{++} \rightarrow \Lambda_c^+ K^- \pi^+ \pi^+$, $\sim 3\%$ from $\Omega_{cc}^{***+} \rightarrow \Xi_{cc}^{++}K^-$ and the rest from direct Ξ_{cc}^{++} production. Finally, using the number of Ξ_{cc}^{++} candidates reconstructed ~ 1500 in [16], we can estimate the number of excited candidates before the selection we are looking for.

$$N(\Xi_{cc}^{***})_{Run2} = 1500 \times 0.3 = 450$$

$$N(\Omega_{cc}^{***})_{Run2} = 1500 \times 0.03 = 45$$

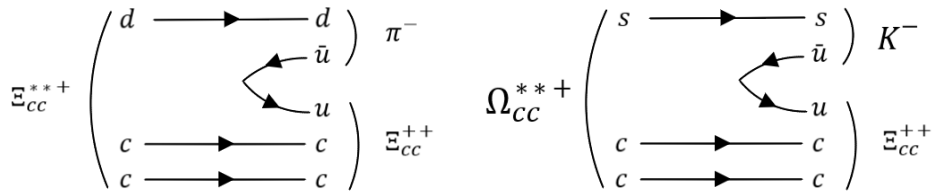


Figure 2: Feynman diagrams of the $\Xi_{cc}^{***+} \rightarrow \Xi_{cc}^{++}\pi^-$ decay on the left and the $\Omega_{cc}^{***+} \rightarrow \Xi_{cc}^{++}K^-$ on the right.

2 Analysis strategy

The analysis searches for the excited states of doubly charmed baryons Ξ_{cc}^{*+} and Ω_{cc}^{*+} through the decay modes $\Xi_{cc}^{***+} \rightarrow \Xi_{cc}^{++}\pi^-$ and $\Omega_{cc}^{***+} \rightarrow \Xi_{cc}^{++}K^-$. The Ξ_{cc}^{++} candidates are reconstructed following previous analysis method through the decay mode $\Xi_{cc}^{++} \rightarrow \Lambda_c^+ K^- \pi^+ \pi^+$ with Λ_c^+ decaying to $pK^-\pi^+$. The reconstructed Λ_c^+ mass is constrained to

be within the region [2270, 2306] MeV/ c^2 , i.e. ± 18 MeV/ c^2 around the known measured value.

First step, reconstruction of Ξ_{cc}^{++} candidates from the exclusive¹ Ξ_{cc}^{++} Turbo line² (see Fig 3a). This step aims to reproduce the results reported in the discovery paper. On top of the trigger selections, further selections that are loose enough to keep almost all signals are applied to reduce the offline tuple size. Then a multivariate selection (MVA) is introduced to fully exploit the difference between signals and backgrounds and to optimize signal significance. The training of the MVA uses simulated signal events and sideband backgrounds in data. Both dataset are from 2016. The cut value is determined by optimizing the signal significance. Then a MVA selector is applied to the the 2016 dataset.

Second step, reconstruction of Ξ_{cc}^{++} candidates from the inclusive Λ_c^+ Turbo line (see Fig 3b). From this trigger all tracks (including pions and kaons) from the PV has been saved and will be necessary for the last step. The process is the same except that the offline selection now include cuts for the Ξ_{cc}^{++} decay, those cuts are chosen to be looser than the ones used from the exclusive line. Moreover the MVA selector will be applied to the full Run2 dataset (2016-2018).

Third step, combine Ξ_{cc}^{++} candidates from the previous step with a pion π^- or a kaon K^- to reconstruct excited doubly charmed baryons candidates. The training of the MVA will use simulated signal events and wrong-sign backgrounds in data.

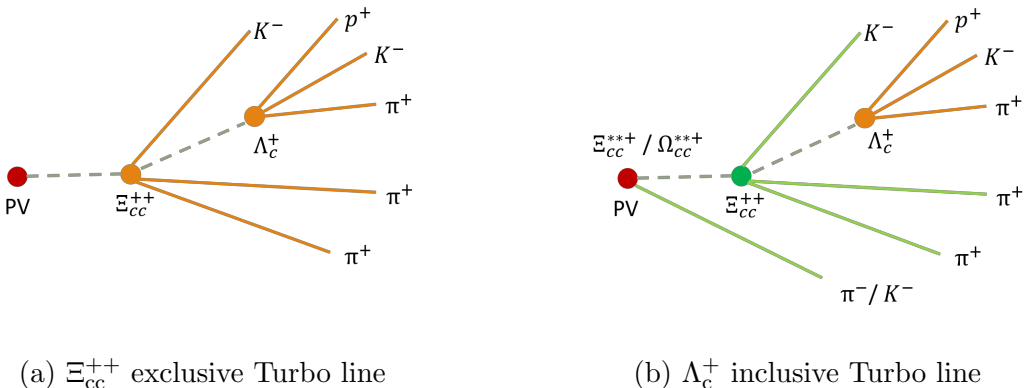


Figure 3: Different type of Turbo line.

¹Only tracks relative to the decay are saved

²A specific type of trigger line (see A.2)

3 Data

3.1 Data

In 2015 the world’s most powerful accelerator (LHC) began its physics programme once again for Run 2, this time with proton beams colliding 13 TeV. For Run 2 data, we use the Turbo output of 2016, 2017 and 2018. The total integrated luminosity is 5.4 fb^{-1} . Turbo output saves the candidates that were reconstructed at the trigger level and makes them available for offline analysis. The bookkeeping locations of the data used are:

3.1.1 $\Xi_{cc}^{++} \rightarrow \Lambda_c^+ K^- \pi^+ \pi^+$ exclusive line

- 2016: Ξ_{cc}^{++} : Hlt2CharmHadXiccpp2LcpKmPipPip_Lcp2PpKmPipTurbo in Turbo03a/94000000/CHARMSPEC PARKED.MDST

3.1.2 $\Lambda_c^+ \rightarrow p^+ K^- \pi^+$ inclusive line

- 2016: Λ_c^+ : Hlt2CharmHadLcpToPpKmPipTurbo in Turbo03a/94000000/CHARMSPEC PARKED.MDST
- 2017: Λ_c^+ : Hlt2CharmHadLcpToPpKmPipTurbo in Turbo04/94000000/CHARMSPEC.MDST
- 2018: Λ_c^+ : Hlt2CharmHadInclLcpToKmPpPipBDTTurbo in Turbo05/94000000/CHARMINCLBARYON.MDST

They are processed with DaVinci v46r5.

4 $\Xi_{cc}^{++} \rightarrow \Lambda_c^+ K^- \pi^+ \pi^+$ exclusive trigger line

4.1 Simulation

In the simulation, pp collisions are generated using PYTHIA [24] with a specific LHCb configuration [25]. A dedicated generator, GENXICC2.0, is used to simulate Ξ_{cc} baryon production [26]. The mass and the lifetime of the Ξ_{cc}^{++} baryon in the simulation are set to be the same as those in Pythia, i.e., $m(\Xi_{cc}^{++}) = 3621.40$ MeV/ c^2 and $\tau(\Xi_{cc}^{++}) = 333$ fs. The Ξ_{cc}^{++} decay products are distributed according to phase space, while the Λ_c^+ decay according to a pseudo-resonant model. The number of simulated events is approximately 2M for each magnet polarity. The bookkeeping locations of the 2016 MC samples are:

```
MC/2016/Beam6500GeV-2016-MagDown-Nu1.6-25ns-GenXiccPythia8/Sim09c/Trig0x6138160F/Reco16/
Turbo03/Stripping28r1NoPrescalingFlagged/26266050/ALLSTREAMS.DST
```

```
MC/2016/Beam6500GeV-2016-MagUp-Nu1.6-25ns-GenXiccPythia8/Sim09c/Trig0x6138160F/Reco16/
Turbo03/Stripping28r1NoPrescalingFlagged/26266050/ALLSTREAMS.DST
```

We used the same MC sample as the original paper. Since then, new MC samples with the mass and lifetime adjusted to the value measured have been generated and can be used instead (done in Sec. 5). Moreover those new MC samples have been also produced under 2017 and 2018 conditions.

4.1.1 MC truth matching

The truth matching is done using true IDs, where we ask for each track to have the correct true ID and come from the true corresponding mother as :

```
abs(Xicc_TRUEID)==4422&abs(Lc_TRUEID)==4122&abs(LcP_TRUEID)==2212
&abs(LcPi_TRUEID)==211&abs(LcK_TRUEID)==321
&(abs(LcP_MC_MOTHER_ID)==4122|abs(LcP_MC_GD_MOTHER_ID)==4122)
&(abs(LcK_MC_MOTHER_ID)==4122|abs(LcK_MC_GD_MOTHER_ID)==4122)
&(abs(LcPi_MC_MOTHER_ID)==4122|abs(LcPi_MC_GD_MOTHER_ID)==4122)
&abs(XiccPi1_TRUEID)==211&abs(XiccPi1_MC_MOTHER_ID)==4422
&abs(XiccPi2_TRUEID)==211&abs(XiccPi2_MC_MOTHER_ID)==4422
&abs(XiccK_TRUEID)==321&abs(XiccK_MC_MOTHER_ID)==4422
```

In fact, even while using simulation particles can be miss-identify because the simulation computes the variables using the detector behaviour model.

Finally the number of events passing pre-selection and MC truth matching are reported in Tab. 1 and the invariant mass distributions are shown in Fig 4.

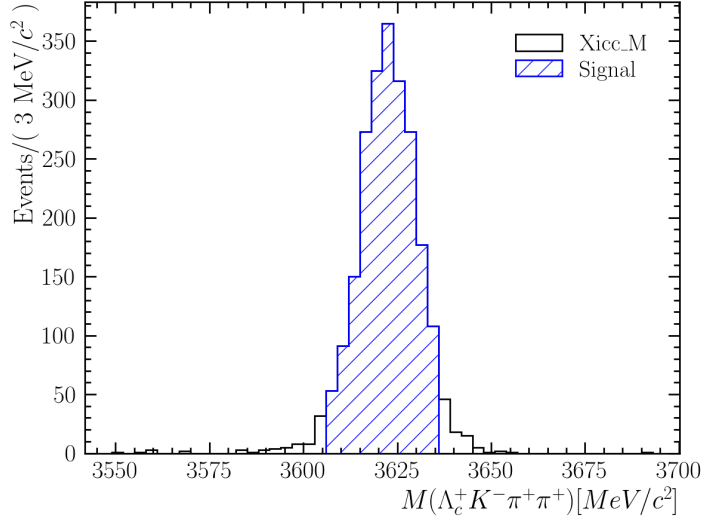


Figure 4: The Ξ_{cc}^{++} mass distribution of MC samples from the exclusive line.

Table 1: Number of MC samples from TURBO tree with different cuts applied.

Tree	Pre-selection	+ MC truth	+ Λ_c^+ and Ξ_{cc}^{++} mass windows
Xicc TURBO	11352	2372	2131

4.2 Selection

The $\Xi_{cc}^{++} \rightarrow \Lambda_c^+ K^- \pi^+ \pi^+$ decay is selected with the following procedure.

- Events are filtered and candidates are reconstructed and selected centrally through the trigger (see Sec. 4.2.1).
- A cut-based pre-selection is applied (see Sec. 4.2.2).
- Candidates are required to lie inside a Λ_c^+ mass window of $2270 < m(\Lambda_c^+) < 2306 \text{ MeV}/c^2$.
- A multivariate selection is applied (see Sec. 4.2.3).

4.2.1 Trigger requirements

For the first step, the Ξ_{cc}^{++} baryon is reconstructed from the Ξ_{cc}^{++} decay products, whose selection is summarized in Tab. 2 and described below.

- $\Lambda_c^+ \rightarrow p^+ K^- \pi^+$ candidates are reconstructed from three long tracks that pass appropriate hadron PID requirements, as well as quality requirements to reject soft and/or prompt tracks ($p_T > 0.2 \text{ GeV}/c$, $p > 1 \text{ GeV}/c$, $\chi^2_{\text{IP}} > 6$). The proton track is required to have momentum $p > 10 \text{ GeV}/c$ (to ensure that it would be above the Cherenkov threshold in RICH1 under the kaon mass hypothesis, otherwise there is no kaon/proton discrimination). To further suppress background, cuts are placed on

combinations of the tracks: at least one of the three tracks must have $p_T > 1 \text{ GeV}/c$ and $\chi^2_{\text{IP}} > 16$, at least two of them must have $p_T > 0.4 \text{ GeV}/c$ and $\chi^2_{\text{IP}} > 9$, and the scalar p_T sum of the three tracks must be greater than $3 \text{ GeV}/c$. The Λ_c^+ candidate must have a good vertex fit quality with $\chi^2_{\text{vtx}}/\text{ndf} < 10$. It must point back to the primary vertex (within 0.01 radian, i.e. $\cos^{-1}(DIRA) < 0.01$), and the vertex should be displaced from primary vertex such that the estimated Λ_c^+ decay time is more than 0.15 ps. Finally, only candidates whose invariant mass is within $\pm 75 \text{ MeV}/c^2$ of the known value are retained.

- $\Xi_{cc}^{++} \rightarrow \Lambda_c^+ K^- \pi^+ \pi^+$ candidates are reconstructed from the Λ_c^+ candidates plus three tracks that pass appropriate hadron PID requirements, as well as having $p_T > 0.5 \text{ GeV}/c^2$ and $p > 1 \text{ GeV}/c$. The vector sum of their p_T is required to be greater than $2 \text{ GeV}/c$. The three tracks and the Λ_c^+ are required to form a vertex: each pairwise combination of the four particles is required to have a distance of closest approach of less than 10 mm, and the fitted Ξ_{cc}^{++} vertex must have $\chi^2_{\text{vtx}}/\text{ndf} < 60$. In addition, the Λ_c^+ decay vertex must be downstream of the Ξ_{cc}^{++} vertex by at least 0.01 mm in the z direction.
- No specific L0 line or HLT1 line are required.

Table 2: HLT2 trigger selections (Ξ_{cc}^{++} exclusive line).

Particles	Variable	Cuts
Daughters of Λ_c^+	Track quality	$\chi^2/ndf < 3$
	Momentum	$p > 1 \text{ GeV}/c$
	Transverse momentum	$p_T > 0.2 \text{ GeV}/c$
	Arithmetic sum of daughter p momentum	$> 3 \text{ GeV}/c$
	Impact parameter significance	$\chi_{IP}^2 > 6$
	p momentum	$p > 10 \text{ GeV}/c$
	p particule ID	$\text{DLL}_{p\pi} > 5, \text{DLL}_{pK} > 5$
	K particule ID	$\text{DLL}_{K\pi} > 5$
	π particule ID	$\text{DLL}_{K\pi} < 5$
	Maximum p_T	$> 1 \text{ GeV}/c$
Λ_c^+	Second maximum p_T	$> 0.4 \text{ GeV}/c$
	Maximum χ_{IP}^2	> 16
	Second maximum χ_{IP}^2	> 9
	Vertex quality	$\chi_{vtx}^2/ndf < 10$
Daughters of Ξ_{cc}^{++}	Cosine of decay angle (DIRA)	$> \cos(0.01)$
	Decay time	$\tau > 0.15 \text{ ps}$
	Mass	$M \pm 75 \text{ MeV}/c^2$
	Track quality	$\chi^2/ndf < 3$
Ξ_{cc}^{++}	Momentum	$p > 1 \text{ GeV}/c$
	Transverse momentum	$p_T > 0.5 \text{ GeV}/c$
	K particule ID	$\text{DLL}_{K\pi} > 10$
	π particule ID	$\text{DLL}_{K\pi} < 0$
Ξ_{cc}^{++}	Vector sum of daughter	$> 2 \text{ GeV}/c$
	Vertex quality	$\chi_{vtx}^2/ndf < 60$
	Λ_c^+ vertex displacement w.r.t. Ξ_{cc}^{++}	$z_{\Lambda_c^+} - z_{\Xi_{cc}^{++}} > 0.01 \text{ mm}$
	Distance of closest approach	$< 10 \text{ mm}$

4.2.2 Offline reconstruction and pre-selection

DecayTreeFitter (DTF) is used to refit to the Ξ_{cc}^{++} candidates. This is necessary for the mass measurement studies (see Sec. 4.2.4) since improves the mass resolution. With DTF, various constraints are possible (such as to constrain the Λ_c^+ mass to its known value, or to constrain the Ξ_{cc}^{++} to originate from the PV). By default we will use a Λ_c^+ mass constraint and PV constraint, unless otherwise stated.

4.2.3 Multivariate selection

After the pre-selection, a multivariate analysis is then used to further improve the expected signal purity. The 2016 data and 2016 MC samples were used for the MVA training, and then applied a MVA cut to 2016 data. In the training, the simulated $\Xi_{cc}^{++} \rightarrow \Lambda_c^+ K^- \pi^+ \pi^+$ events after the pre-selection and truth matching are used as signals, the upper sideband data within $(3800, 3900) \text{ MeV}/c^2$ with the same pre-selection applied is used as backgrounds. Due to the large sample size of the background, only part of the background

is used in the training and the testing, and the remaining will be used in the working point significance estimation. Following a standard TMVA approach, both the signal and background samples were split randomly into two equally sized disjoint subsamples, one for the training and the other for the testing. The analysis used the same variable list as the discovery paper. Given the limited sample size of the signal MC sample, they have limited the number of variables to reduce the risk overtraining. The 10 variables used for the training are listed in Tab. 3. Their distributions are shown in Fig. 5. Their correlation matrices are shown in Fig. 6. The boosted decision tree (BDT and BDTG) based and the multilayer perceptron (MLP) based selectors were considered to give the best performance according to the previous analysis. The Receiver Operating Characteristic (ROC) curves of these three selectors are shown in Fig. 7, and the MVA output distributions are shown in Fig. 8.

Since the decay mode is already observed, the working point is determined by optimizing the signal significance. For a cut t on the output, the signal significance is defined as

$$\text{signal significance } (t) = \frac{S(t)}{\sqrt{S(t) + B(t)}} \quad (1)$$

where S is the expected number of signals determined from MC samples, and B is the expected number of backgrounds determined from sideband region. Both S and B are evaluated as

$$S(t) = \frac{\text{No. of signal events passing full selection in MC samples}}{C_{MC-data}} \quad (2)$$

$$B(t) = \frac{\text{No. of background events passing the full selection}}{C_{window}} \quad (3)$$

The scaling factors are:

- $C_{MC-data}$ is a scale factor to scale the size of MC samples into Data samples. This scale factor is calculated by $\frac{\text{Yield in data}}{\text{Yield in MC}}$ and we need to have an estimated MVA cut first to obtain the yields. When cut at an estimated point (0.05 of the BDT response in this case), the number of signal candidates passed in MC samples is 2136 and in Data samples is 330. So the scale factor is found to be $2131/330 = 6.46$.
- C_{window} is the scale factor to scale the size of upper sideband data into RS. In this case, the upper sideband data used here is within $(3800, 3900)$ MeV/ c^2 and the mass window is ± 15 MeV/ c^2 . So it is found to be $100/30 = 3.33$. This scale factor is just an estimation because the background shape is not accurately flat. When considering the shape of the background, the working point changes little. It's also expected not to vary significantly since the working point is determined in a region where the signal significance is flat versus BDT response values. So, $C_{window} = 3.33$ is good enough for an estimation.

The variation of the signal significance is shown for different selectors in Fig. 9, and the optimal values are shown in Tab. 4. The three selectors give similar performances according to the maximum significance calculated from their training performances. Then,

the optimal cuts from Tab. 4 have been applied on the full 2016 Data samples and the local significance have been calculated again. It used the same definition as Eq. 4 but the signal and background yield are measured from the model fit. The number of candidates is calculated by integrating the signal (or background) PDF (described in Sec. 4.2.4) over an interval of $\mu \pm 2.5\sigma$. The resulting significances are reported in Tab. 5. The 12σ significance reported by the discovery paper is achieved by all the selectors and the MLP selector shows again the best performance. Therefore, the MLP is used in later analysis. The working point we use is a cut $t > 0.353$. The number of candidates drops to 20200.

Table 3: The 10 variables used in MVA selectors.

1.	$\log(\chi_{IP}^2)$ of Ξ_{cc}^{++} to its PV
2.	$\cos^{-1}(\text{DIRA})$ of Ξ_{cc}^{++} from its PV
3.	$\log(\text{FD}\chi^2)$ of Ξ_{cc}^{++} from its PV
4.	χ_{vtx}^2/ndf of the Λ_c^+ vertex fit
5.	χ_{vtx}^2/ndf of the Ξ_{cc}^{++} vertex fit (non-DTF)
6.	χ_{vtx}^2/ndf of the Ξ_{cc}^{++} vertex fit (DTF, with the PV constraint)
7.	Smallest $\log(\chi_{IP}^2)$ among the daughters (Λ_c^+ , K^- , π^+ and π^+) of Ξ_{cc}^{++}
8.	Scalar p_T sum of the daughters (Λ_c^+ , K^- , π^+ and π^+) of Ξ_{cc}^{++}
9.	Smallest p_T among the daughters (Λ_c^+ , K^- , π^+ and π^+) of Ξ_{cc}^{++}
10.	Smallest p_T among the final daughters of the Λ_c^+

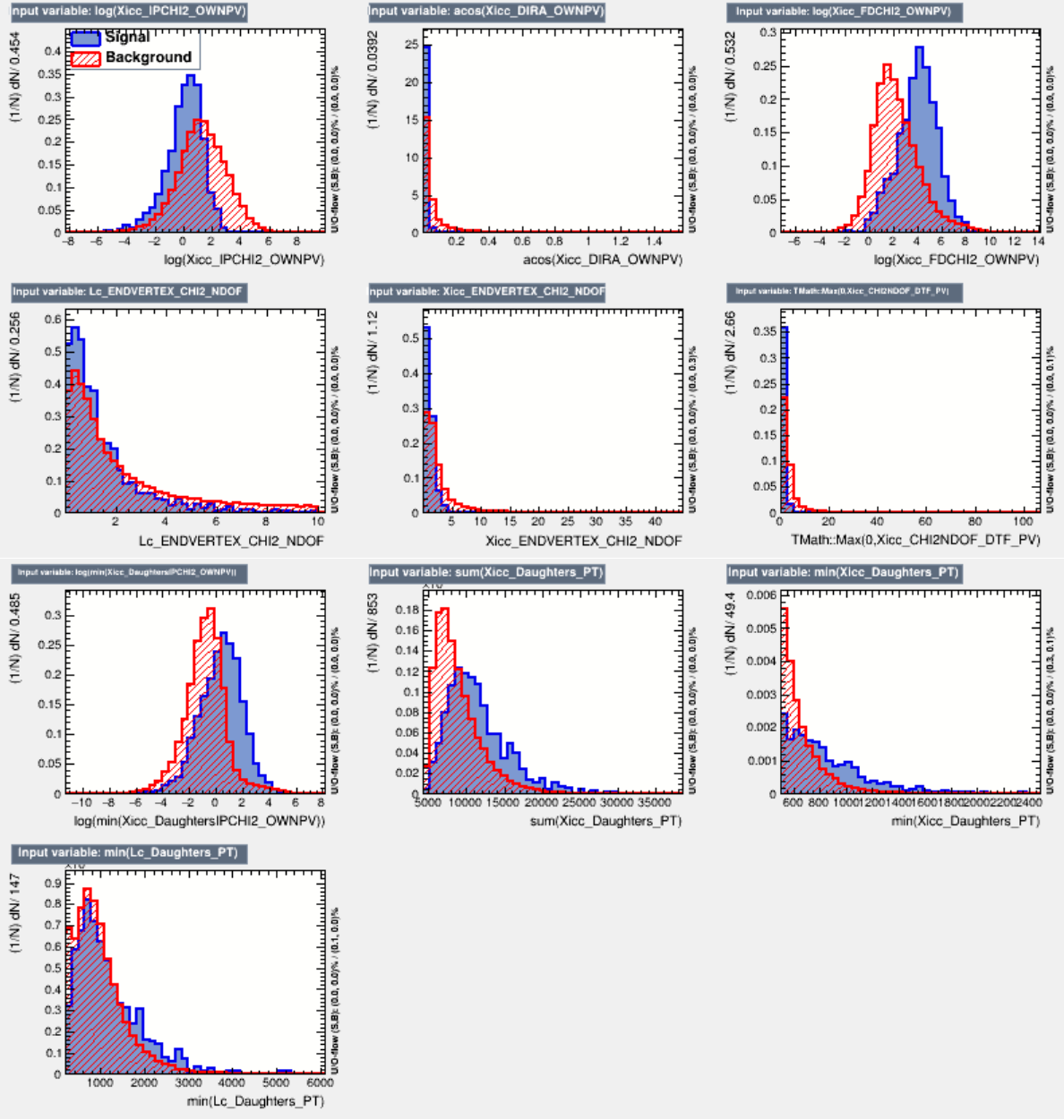


Figure 5: Distributions of input variables, compared between (blue) signals and (red) backgrounds.

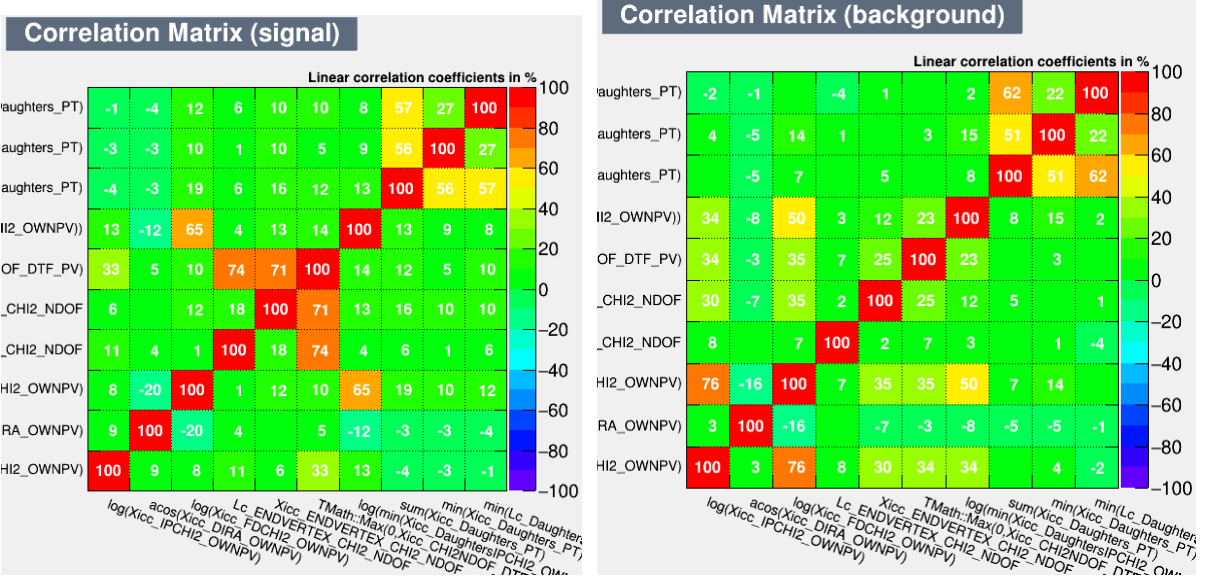


Figure 6: Correlation matrices for the 10 variables used in the multivariate selector, for (left) signal and (right) background.

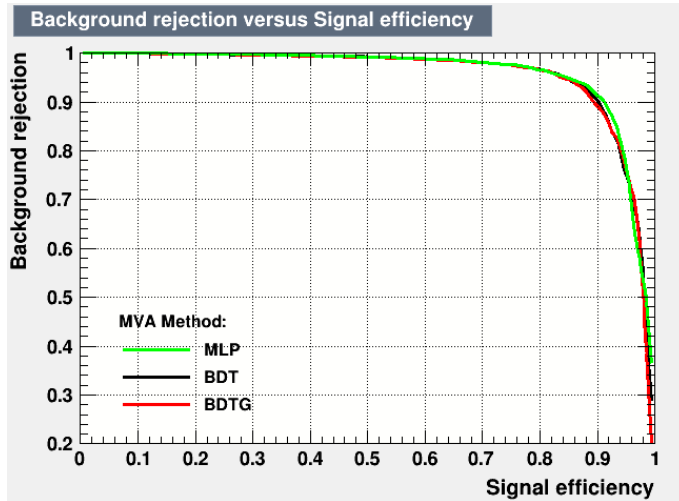


Figure 7: ROC curves for MVA selectors. The vertical axis shows the background rejection fraction, and the horizontal the signal efficiency.

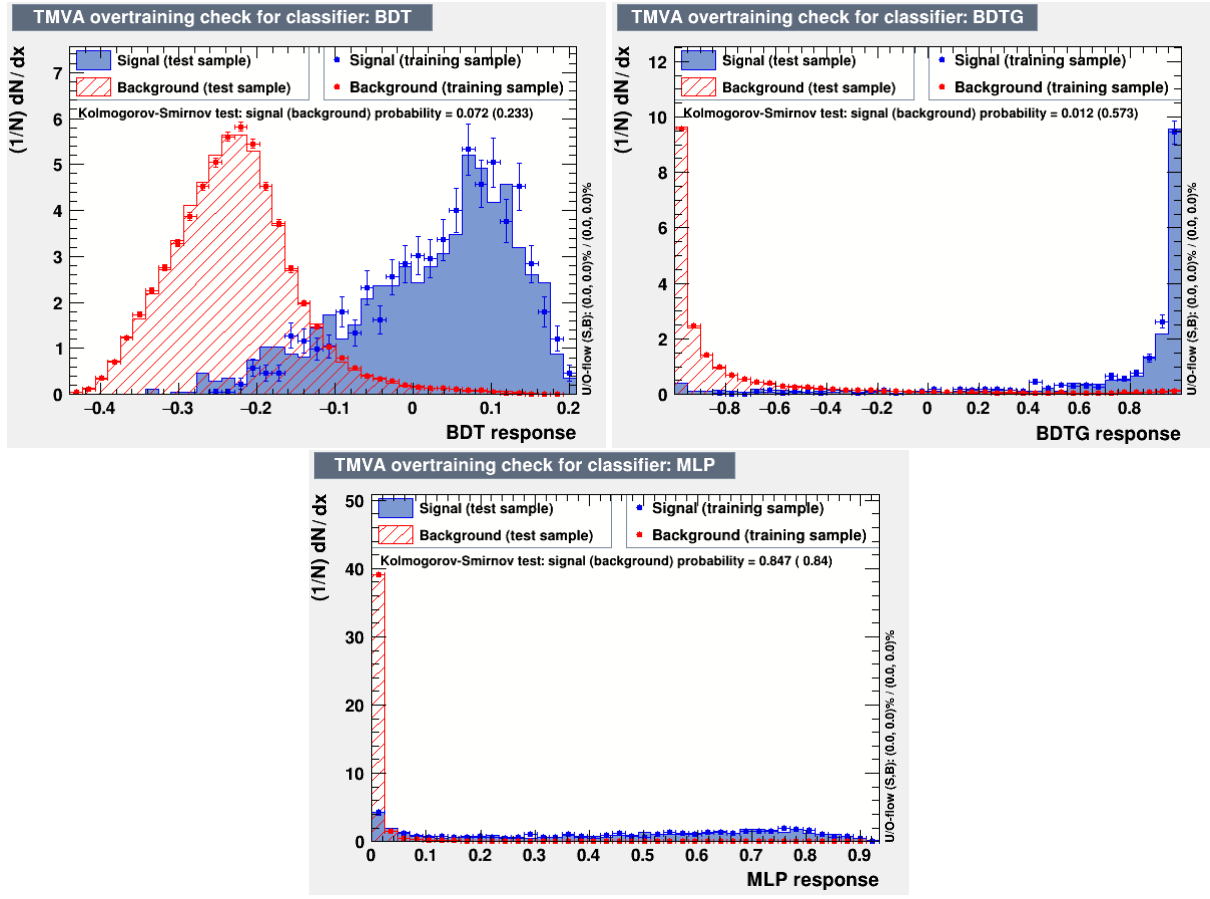


Figure 8: Response curves for MVA selectors: (top left) BDT, (top right) BDTG, (bottom) MLP. For each plot, the horizontal axis shows the MVA output and the vertical axis shows the normalised distribution. The output for the training sample is shown as points with error bars and the output for the test sample is shown as a shaded/hatched histogram.

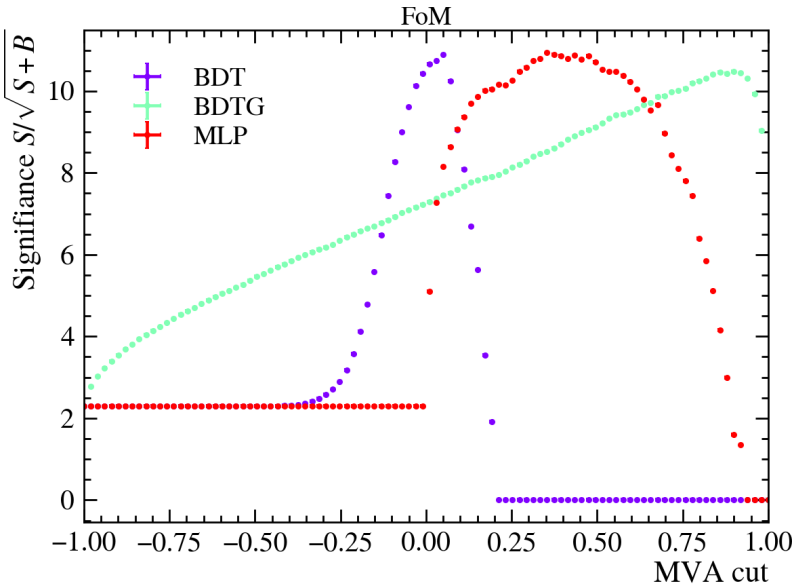


Figure 9: Dependence of the signal significance on the cut applied, for three different selectors.

Table 4: The optimal working points for various MVA selectors, and the signal efficiency and FOM values at those working points.

Selector	Optimal cut	Signal efficiency	Significance
BDT	0.050	0.51	10.89 σ
BDTG	0.899	0.59	10.49 σ
MLP	0.353	0.64	10.94 σ

Table 5: The signal yield, background yield and the corresponding local significance at the working points determined above.

MVA Cut	Signal yield	Background yield	Significance
BDT > 0.050	329.8	438.1	11.9 σ
BDTG > 0.899	423.7	789.2	12.2 σ
MLP > 0.353	485.4	973.4	12.7 σ

4.2.4 Measurement of the Ξ_{cc}^{++} mass

Fig. 10 shows an unbinned extended maximum likelihood fit to the invariant mass distribution of the 2016 data in the mass range $3620 \pm 150 \text{ MeV}/c^2$. In the fit the signal distribution is described by a Gaussian and the background is modelled by an exponential. The mean value of the signal component is $\mu = 3621.8 \pm 0.6 \text{ MeV}/c^2$, the mass resolution is $\sigma = 6.8 \pm 0.8 \text{ MeV}/c^2$ and the background slope is 0.00200 ± 0.00012 . The signal yield is 485 ± 45 and the background yield is 8756 ± 100 in the $\pm 150 \text{ MeV}/c^2$ mass window and 973 in the $\pm 2.5\sigma$ mass window.

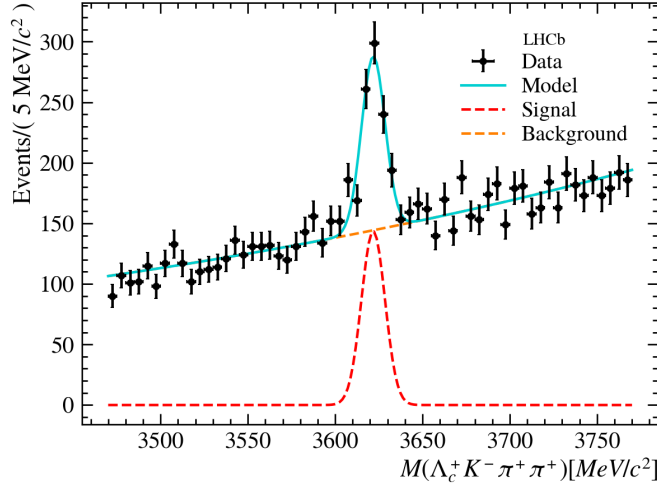


Figure 10: Fit to the invariant mass distribution for the 2016 sample around the mass peak.

We can apply a tighter cut on the data to match the background level with the one from the discovery paper. The two plots are shown side by side in Fig. 11 and look similar.

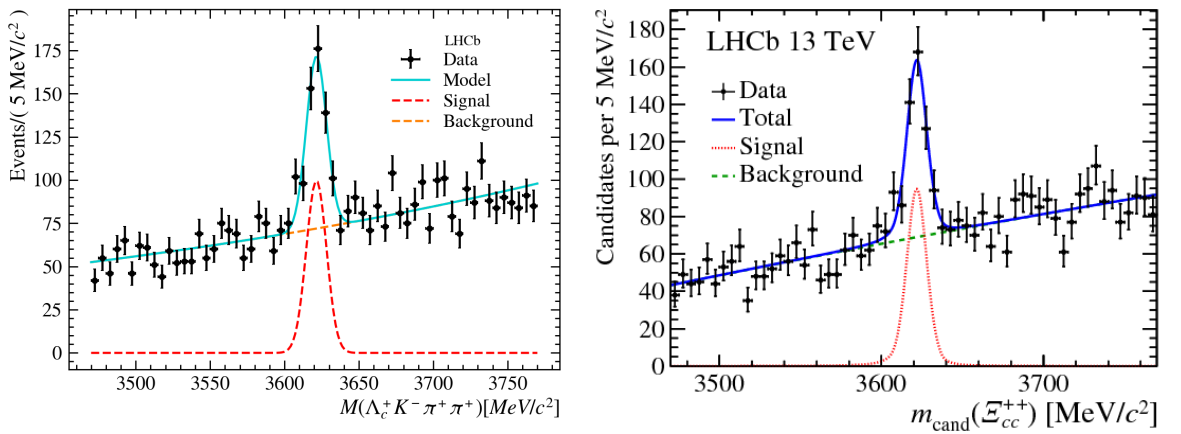


Figure 11: On the left, Ξ_{cc}^{++} mass distribution from our analysis with a tighter MLP cut ($MLP > 0.5$) to reduce the background level. On the right, Ξ_{cc}^{++} mass distribution from the discovery paper using 2016 Data.

5 $\Xi_{cc}^{++} \rightarrow \Lambda_c^+ K^- \pi^+ \pi^+$ inclusive line

5.1 Simulation

In the simulation, pp collisions are generated under the same conditions as Sec. 4.1. But the lifetime have been adjusted to measured value. The mass and the lifetime of the Ξ_{cc}^{++} baryon in the simulation are set to be the same as those in Pythia, i.e., $m(\Xi_{cc}^{++}) = 3621.40$ MeV/ c^2 and $\tau(\Xi_{cc}^{++}) = 256$ fs. The number of simulated events is approximately 0.5M for each magnet polarity therefore we are using MC samples from 2016, 2017 and 2018 to get more candidates. The bookkeeping locations of the MagnetDown MC samples are:

MC/2016/Beam6500GeV-2016-MagDown-Nu1.6-25ns-GenXiccPythia8/Sim10a/Trig0x6139160F/Reco16/Turbo03a/Stripping28r2NoPrescalingFlagged/26266052/ALLSTREAMS.MDST

MC/2017/Beam6500GeV-2017-MagDown-Nu1.6-25ns-GenXiccPythia8/Sim10a/Trig0x62661709/Reco17/Turbo04a-WithTurcal/Stripping29r2NoPrescalingFlagged/26266052/ALLSTREAMS.MDST

MC/2018/Beam6500GeV-2018-MagDown-Nu1.6-25ns-GenXiccPythia8/Sim10a/Trig0x617d18a4/Reco18/Turbo05-WithTurcal/Stripping34NoPrescalingFlagged/26266052/ALLSTREAMS.MDST

5.1.1 MC truth matching

The truth matching is done using true IDs, where we ask for each track to have the correct true ID and come from the true corresponding mother as in Sec .4.1.1.

Finally the number of events passing pre-selection and MC truth matching is 3051 and the invariant mass distribution is shown in Fig 12.

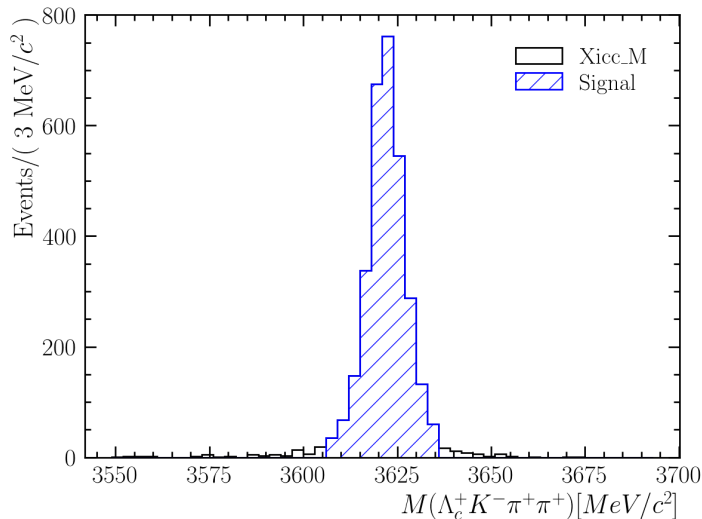


Figure 12: The Ξ_{cc}^{++} mass distribution of MC samples from the inclusive line.

5.2 Selection

The $\Xi_{cc}^{++} \rightarrow \Lambda_c^+ K^- \pi^+ \pi^+$ decay is selected with the same procedure but now the trigger selection only reconstructed the Λ_c^+ candidates. Therefore, the Ξ_{cc}^{++} candidates are

reconstructed through an offline selection. Finally, clone and duplicated candidates are removed.

- Events are filtered and candidates are reconstructed and selected centrally through the trigger (see Sec. 5.2.1).
- A cut-based pre-selection is applied (see Sec. 5.2.2).
- Candidates are required to lie inside a Λ_c^+ mass window of $2270 < m(\Lambda_c^+) < 2306 \text{ MeV}/c^2$.
- A multivariate selection is applied (see Sec. 5.2.3).
- Clone and duplicated candidates are removed (see Sec. 5.2.4).

5.2.1 Trigger requirements

The trigger requirements for the Λ_c^+ candidates and daughters are the same as the paper [16]. Only the requirements for Ξ_{cc}^{++} candidates and daughters have changed and are described in Sec. 5.2.2.

Table 6: Hlt2 trigger selection (Λ_c^+ inclusive line).

Particles	Variable	Cuts
Daughters of Λ_c^+	Track quality	$\chi^2/ndf < 3$
	Momentum	$p > \text{GeV}/c$
	Transverse momentum	$p_T > 0.2 \text{ GeV}/c$
	Arithmetic sum of daughter p momentum	$> 3 \text{ GeV}/c$
	Impact parameter significance	$\chi_{IP}^2 > 6$
	p momentum	$p > 10 \text{ GeV}/c$
	p particle ID	$\text{DLL}_{p\pi} > 5, \text{DLL}_{pK} > 5$
	K particle ID	$\text{DLL}_{K\pi} > 5$
	π particle ID	$\text{DLL}_{K\pi} < 5$
	Maximum p_T	$> 1 \text{ GeV}/c$
	Second maximum p_T	$> 0.4 \text{ GeV}/c$
	Maximum χ_{IP}^2	> 16
Λ_c^+	Second maximum χ_{IP}^2	> 9
	Vertex quality	$\chi_{vtx}^2/ndf < 10$
	Cosine of decay angle (DIRA)	$> \cos(0.01)$
	Decay time	$\tau > 0.15 \text{ ps}$
	Mass	$M \pm 75 \text{ MeV}/c^2$

Differences in 2017 and 2018 The authors of the paper [16] has claimed 'problems' while using this line in 2017 and 2018. After investigation, we found out that few changes have been made in the Λ_c^+ trigger line in 2017 and 2018 (See Tab. 7). The cuts on the companion tracks χ_{IP}^2 remove about the half of the Ξ_{cc}^{++} candidates (red line) as we can see on Fig. 13. While the cuts on Λ_c^+ candidates have little impact on the selection (See

Fig. 14). In 2017, no alternative line is available so the efficiency is reduced and in 2018, we switched to an another inclusive line with the same cuts as in 2016 (See Sec. 3.1.2)

Table 7: Hlt2 trigger selection differences for 2017 and 2018.

Particles	Variable	Cuts
Λ_c^+	Impact parameter significance	$\chi_{IP}^2 < 15$
	Decay time	$\tau > 0.30 \text{ ps}$
	Momentum	$p > 30 \text{ GeV}/c$
	Transverse momentum	$p_T > 2 \text{ GeV}/c$
Companion tracks	Track quality	$\chi^2/ndf < 3$
	Ghost probability	$GhostProb < 0.4$
	Impact parameter significance	$\chi_{IP}^2 < 15$
	Momentum	$p > 1 \text{ GeV}/c$
	Transverse momentum	$p_T > 0.2 \text{ GeV}/c$

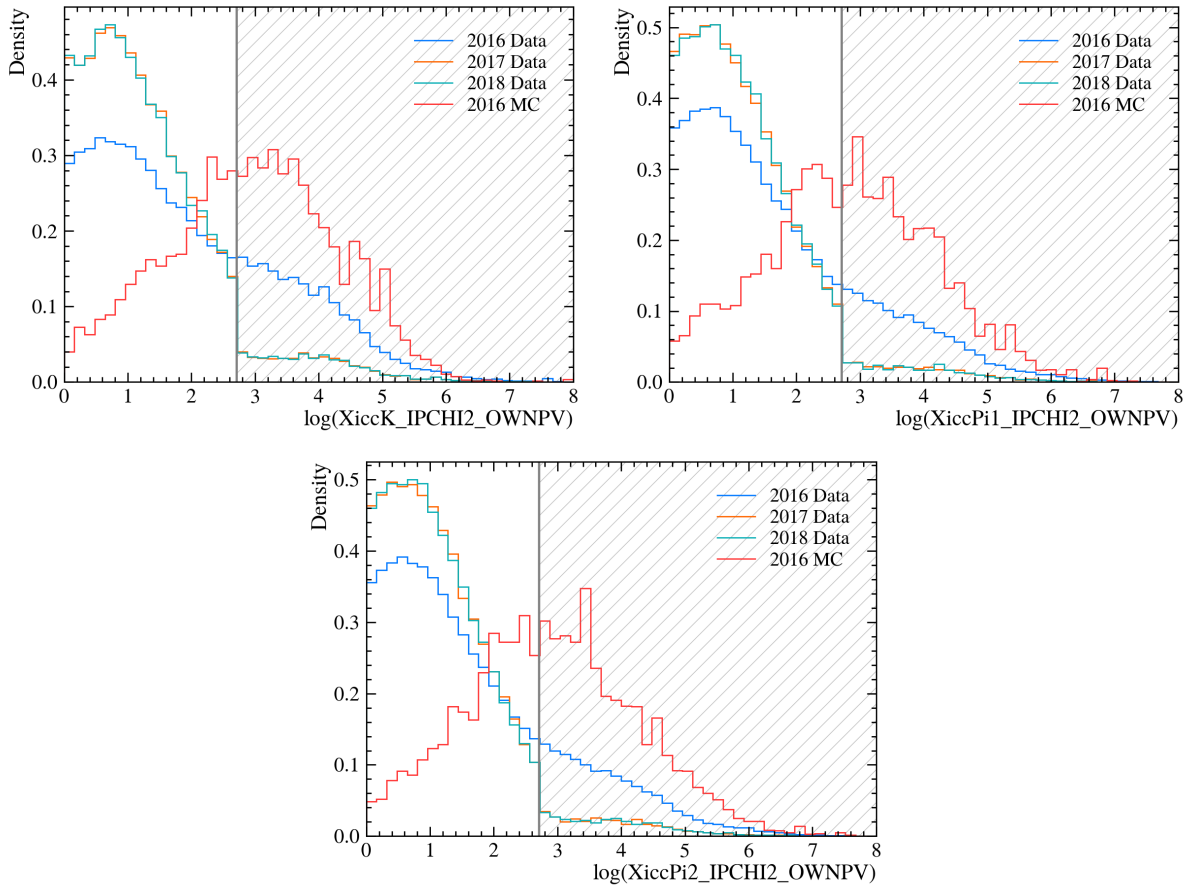


Figure 13: Companion tracks χ_{IP}^2 selection cuts.

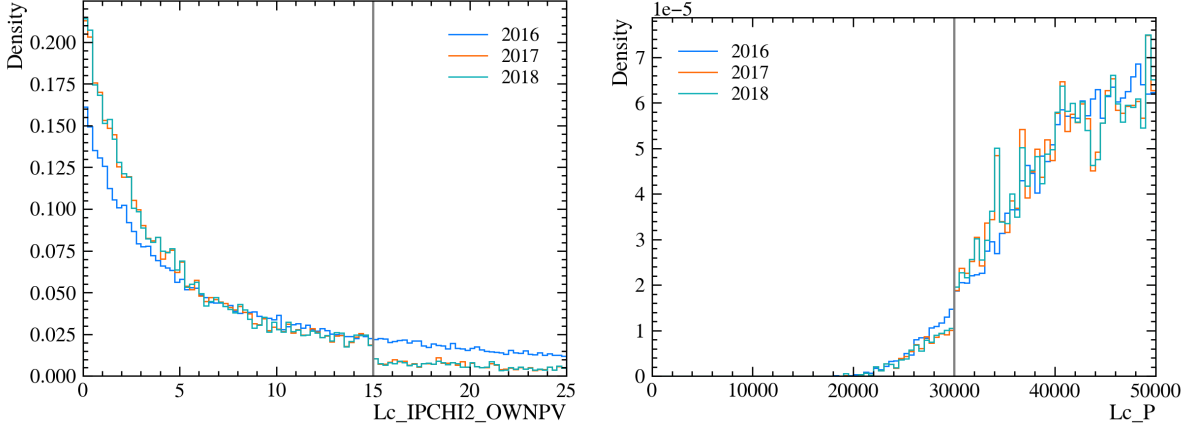


Figure 14: Λ_c^+ selection cuts (χ_{IP}^2 on the left, p on the right).

5.2.2 Offline reconstruction and pre-selection

$\Xi_{cc}^{++} \rightarrow \Lambda_c^+ K^- \pi^+ \pi^+$ candidates are reconstructed from the Λ_c^+ candidates plus three tracks that pass appropriate hadron PID requirements, those cuts are looser than the ones used for the exclusive line, as well as having $p_T > 0.25 \text{ GeV}/c$ for K^- and $p_T > 0.2 \text{ GeV}/c$ for π^+ . The vector sum of their p_T is required to be greater than $2 \text{ GeV}/c$. The three tracks and the Λ_c^+ are required to form a vertex, and the fitted Ξ_{cc}^{++} vertex must have $\chi_{vtx}^2/\text{ndf} < 25$. The reconstructed Ξ_{cc}^{++} candidates is required to come from the primary vertex, by imposing pointing requirements (DIRA and χ_{IP}^2). The selection for the $\Xi_{cc}^{++} \rightarrow \Lambda_c^+ K^- \pi^+ \pi^+$ is summarized in Tab. 8.

Table 8: Offline selection for the $\Xi_{cc}^{++} \rightarrow \Lambda_c^+ K^- \pi^+ \pi^+$ decay.

Particles	Variable	Cuts
Daughters of Ξ_{cc}^{++}	Track quality	$\chi^2/\text{ndf} < 3$
	Ghost Probability	< 0.4
	Impact parameter	$\chi_{IP}^2 > 1$
	Transverse momentum	$p_T(\pi) > 0.2 \text{ GeV}/c$
	Transverse momentum	$p_T(K^+) > 0.25 \text{ GeV}/c$
	K particle ID	$ProbNNk > 0.1$
	π particle ID	$ProbNNpi > 0.2$
Ξ_{cc}^{++}	Vector sum of daughter	$> 2 \text{ GeV}/c$
	Vertex quality	$\chi_{vtx}^2/\text{ndf} < 25$
	Impact parameter χ^2	$\chi_{IP}^2 < 25$
	Pointing angle	DIRA > 0.99

DecayTreeFitter (DTF) is also used to refit to the Ξ_{cc}^{++} candidates to constrain the Λ_c^+ mass to its known value and to constrain the Ξ_{cc}^{++} to originate from the PV.

5.2.3 Multivariate selection

After the pre-selection, a multivariate analysis is then used to further improve the expected signal purity. The 2016 data and Run2 MC samples were used for the MVA training, and then applied a MVA cut to Run2 data. In the training, the simulated $\Xi_{cc}^{++} \rightarrow \Lambda_c^+ K^- \pi^+ \pi^+$ events after the pre-selection and truth matching are used as signals, the upper sideband data within $(3800, 3900)$ MeV/ c^2 with the same pre-selection applied is used as backgrounds. Due to the large sample size of the background, only part of the background is used in the training and the testing, and the remaining will be used in the working point significance estimation. Following a standard TMVA approach, both the signal and background samples were split randomly into two equally sized disjoint subsamples, one for the training and the other for the testing. The number of MC signal candidates is larger for this reconstruction line due to the looser cuts. Therefore, we can use a larger number of variables for the MVA selectors. We will use the 21 variables listed in Tab. 9. This is the same set of MVA variables as [16] apart for few changes. In fact, we have used the sum and absolute difference of the two pions variables coming from the Ξ_{cc}^{++} instead of the raw value to be invariant by the exchange of the two pions (i.e. $\pi_1 \longleftrightarrow \pi_2$). Their distributions are shown in Fig. 15. Their correlation matrices are shown in Fig. 16. The boosted decision tree (BDT and BDTG) based and the multilayer perceptron (MLP) based selectors were considered to give the best performance according to the previous analysis. The Receiver Operating Characteristic (ROC) curves of these three selectors are shown in Fig. 17, and the MVA output distributions are shown in Fig. 18.

Table 9: The 21 variables used in MVA selectors.

-
1. $\log(\chi_{\text{IP}}^2)$ of Ξ_{cc}^{++} to its PV
 2. $\cos^{-1}(\text{DIRA})$ of Ξ_{cc}^{++} from its PV
 3. $\log(\chi_{\text{FD}}^2)$ of Ξ_{cc}^{++} from its PV
 4. $\chi_{\text{vtx}}^2/\text{ndf}$ of the Λ_c^+ vertex fit
 5. $\log(\chi_{\text{vtx}}^2/\text{ndf})$ of the Ξ_{cc}^{++} vertex fit (non-DTF)
 6. $\log(\chi_{\text{vtx}}^2/\text{ndf})$ of the Ξ_{cc}^{++} vertex fit (DTF, with the PV constraint)
 7. PID _{p} of the p from Λ_c^+
 8. PID _{K} of the K^- from Λ_c^+
 9. PID _{K} of the π^+ from Λ_c^+
 10. PID _{K} of the K^- from Ξ_{cc}^{++}
 11. Sum of PID _{K} of the two π^+ from Ξ_{cc}^{++}
 12. Absolute difference of PID _{K} of the two π^+ from Ξ_{cc}^{++}
 13. Smallest p_T among the daughters (Λ_c^+ , K^- , π^+ and π^+) of Ξ_{cc}^{++}
 14. Scalar p_T of Λ_c^+
 15. Sum of p_T of the two π^+ from Ξ_{cc}^{++}
 16. Absolute difference of p_T of the two π^+ from Ξ_{cc}^{++}
 17. Scalar p_T of the K^- from Ξ_{cc}^{++}
 18. $\log(\chi_{\text{IP}}^2)$ of Λ_c^+
 19. $\log(\chi_{\text{IP}}^2)$ of the K^- from Ξ_{cc}^{++}
 20. log sum of χ_{IP}^2 of the two π^+ from Ξ_{cc}^{++}
 21. log absolute difference χ_{IP}^2 of the two π^+ from Ξ_{cc}^{++}
-

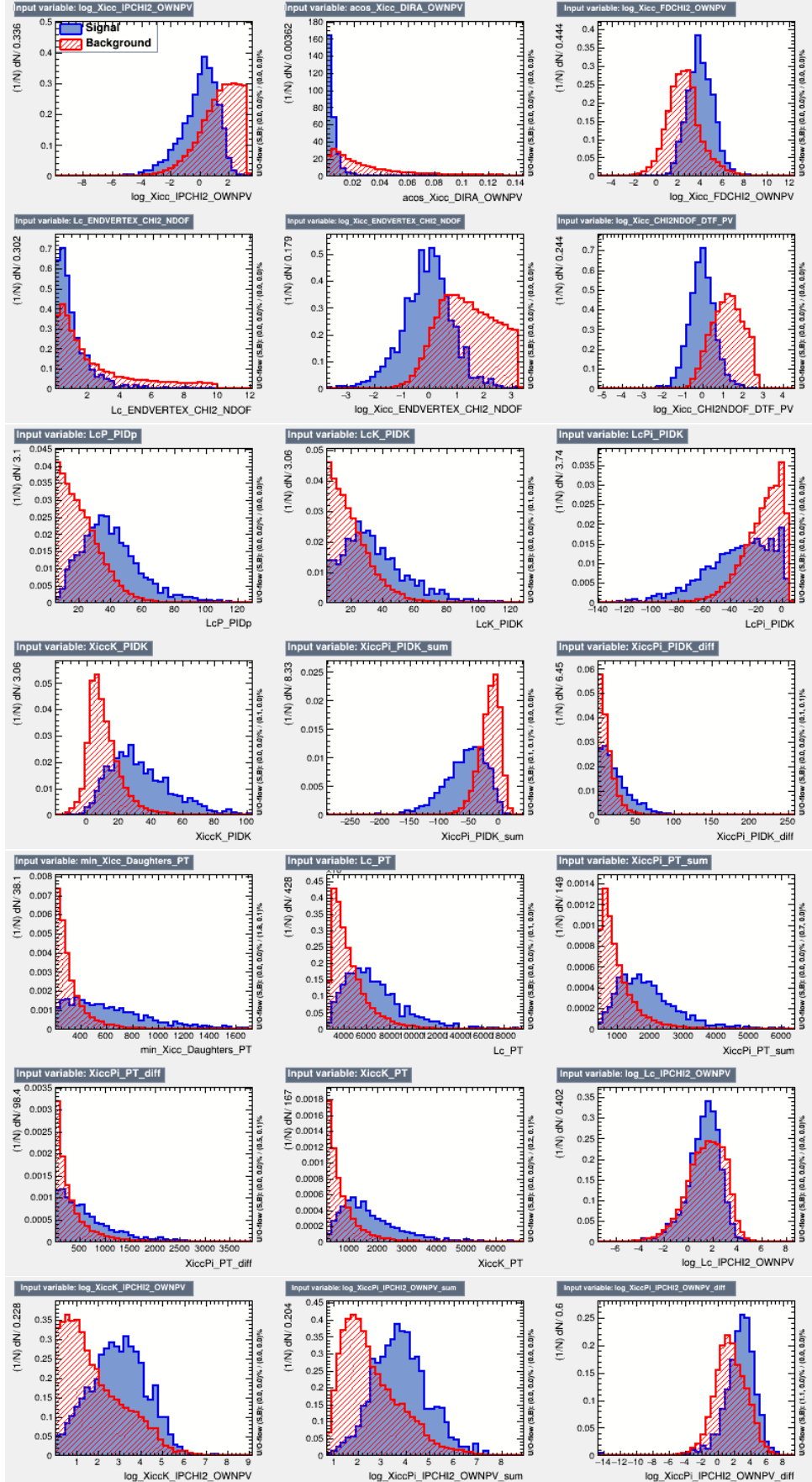


Figure 15: Distributions of input variables compared between (blue) signals and (red) backgrounds.

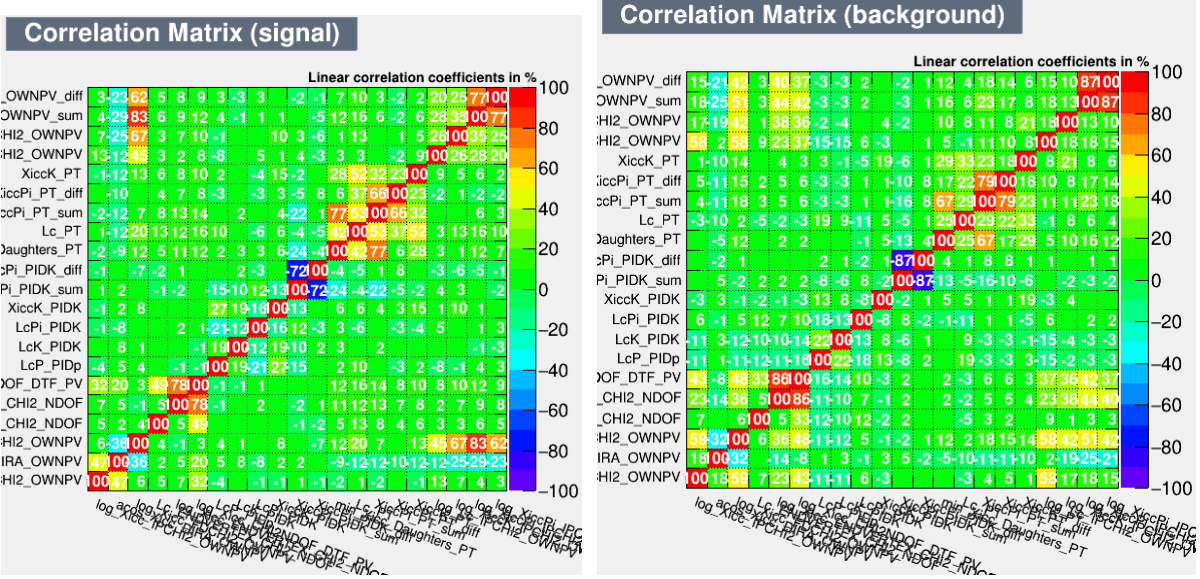


Figure 16: Correlation matrices for the 21 variables used in the multivariate selector, for (left) signal and (right) background.

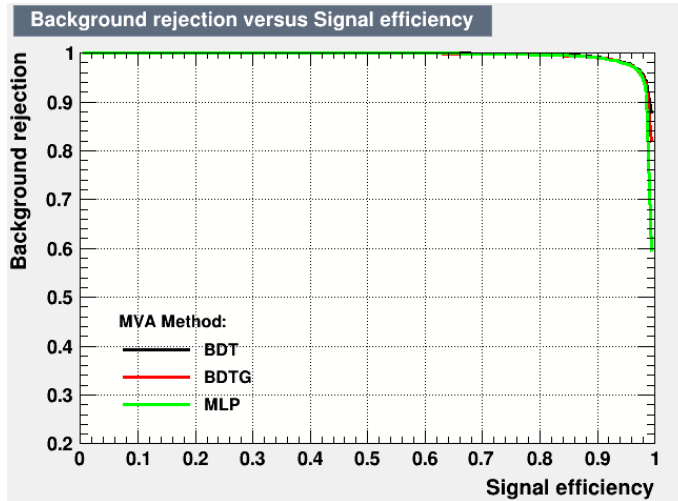


Figure 17: ROC curves for MVA selectors. The vertical axis shows the background rejection fraction, and the horizontal the signal efficiency.

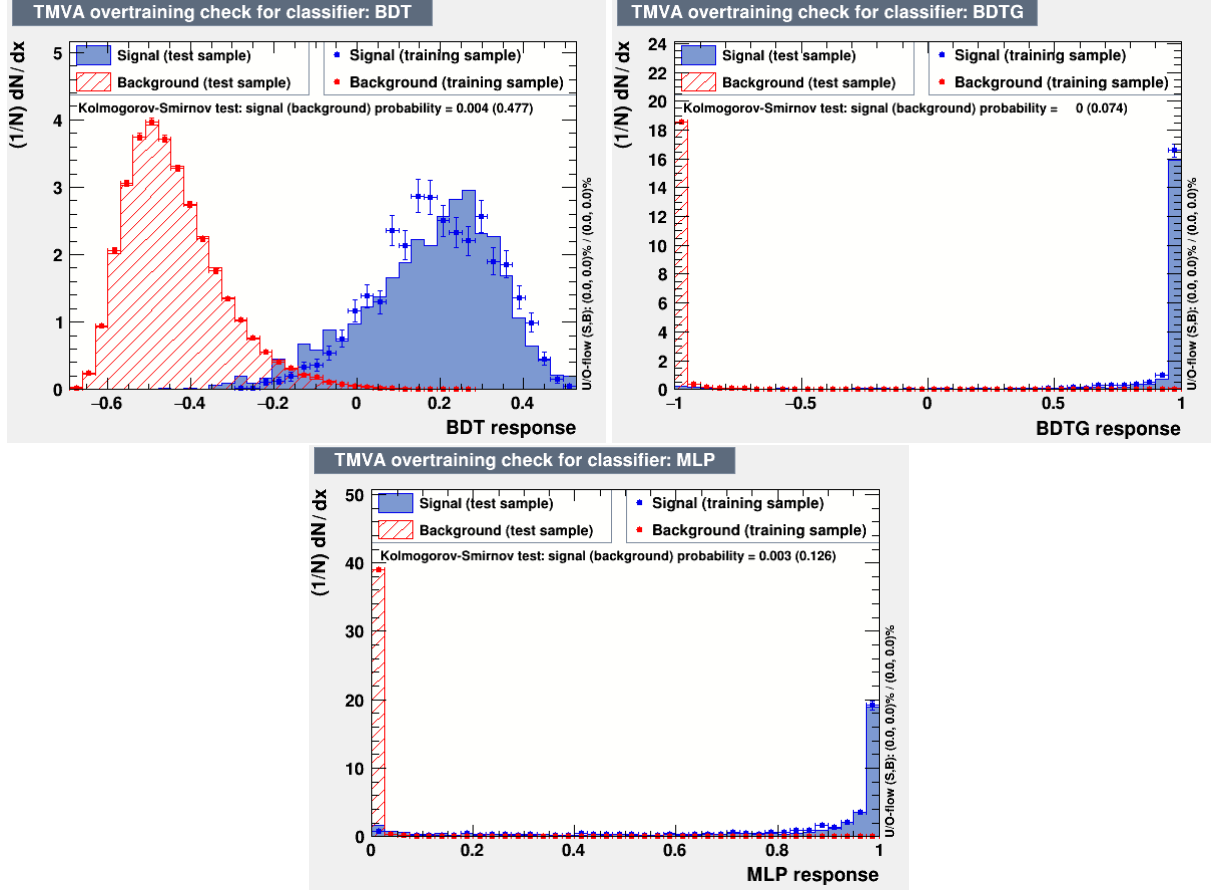


Figure 18: Response curves for MVA selectors: (top left) BDT, (top right) BDTG, (bottom) MLP. For each plot, the horizontal axis shows the MVA output and the vertical axis shows the normalised distribution. The output for the training sample is shown as points with error bars and the output for the test sample is shown as a shaded/hatched histogram.

5.2.4 Removal of internal track clone candidates and duplicated candidates

In order to study these candidates, first we define identical "tracks" as below:

- If two tracks are in the same event and they have an open angle smaller than 0.5 mrad and a momentum difference smaller than 5 tracks.

We can't use the *TRACK_KEY* because the different tracks aren't from the same container and in 2016 there was a bug that caused tracks to be saved several times with different *TRACK_KEY*. (This explains the higher number of duplicated candidates in 2016 in Tab. 10)

Internal track clone candidates There is a special case of the background: among the six tracks that are used to reconstruct Ξ_{cc}^{++} candidates, at least one pair of them are clones of each other, e.g., a track of the pion from Λ_c^+ may be reconstructed twice, and the clone one is assigned to the pion from Ξ_{cc}^{++} .

By requiring all pairs of tracks to be different according to the previous definition, these background contributions are removed.

Removal of duplicated candidates Since in the $\Xi_{cc}^{++} \rightarrow \Lambda_c^+ K^- \pi^+ \pi^+$ decay there are six tracks in the final state, the level of multiple candidates is not expected to be small, due to multiple combinations from a lot of tracks in same events.

Duplicated candidates refers to those candidates who share all the tracks. The simplest example is that the tracks from the two pions who come directly from Ξ_{cc}^{++} are swapped, so a duplicated candidate is formed, as shown in Fig. 9. More general duplicated candidates are removed by the following strategy:

- If two Ξ_{cc}^{++} candidates (the same for more than two candidates) share six pairs of identical final-state tracks, only one candidate is kept, randomly selected among the candidates.
- If two Ξ_{cc}^{++} candidates do not share all the tracks, they are not affected by multiple candidate removal in this procedure.

Tab. 10 shows the number of removed duplicated candidates who shares all six tracks. Since we only remove perfect duplicated candidates, there is still about 10% candidates sharing Λ_c^+ .

Year	Yields before removal	Removed clone	Removed duplication	Yields after removal
2016	154034	-487 (0.32%)	-62776 (-40.88%)	90771 (58.93%)
2017	51987	-116 (0.22%)	-2260 (-4.36%)	49611 (95.43%)
2018	112089	-351 (0.31%)	-5931 (-5.31%)	105807 (94.40%)

Table 10: Yields and number of removed clone and duplicated candidates in 2016-2018 data ($BDT > 0$).

5.3 Significance optimization and mass fit

Fig. 19 shows the signal significance dependence over the BDT cut computed from the real data. The optimal cut is $BDT > 0.07$. The significance is computed using the number of signal events and background events in a $\pm 2.5\sigma$ window from the fitting results on the real data. Fig. 20 shows an unbinned extended maximum likelihood fit to the invariant mass distribution of the Run2 data in the mass range $3620 \pm 150 \text{ MeV}/c^2$. In the fit the signal distribution is described by a Gaussian and the background is modelled by an exponential. The mean value of the signal component is $\mu = 3622.32 \pm 0.24 \text{ MeV}/c^2$, the mass resolution is $\sigma = 5.59 \pm 0.26 \text{ MeV}/c^2$. The signal yield is 2488 ± 99 and the background yield is 60324 ± 260 in the $\pm 150 \text{ MeV}/c^2$ mass window. And finally, Fig. 21 shows our results, with a tighter cut in order to match the signal purity of the mass measurement paper [16], compare to their results. We get a lower number of candidates because of the low efficiency in 2017 (they have used the exclusive line (Sec. 4) to overcome the efficiency issue in 2017, report in Sec. 5.2.1).

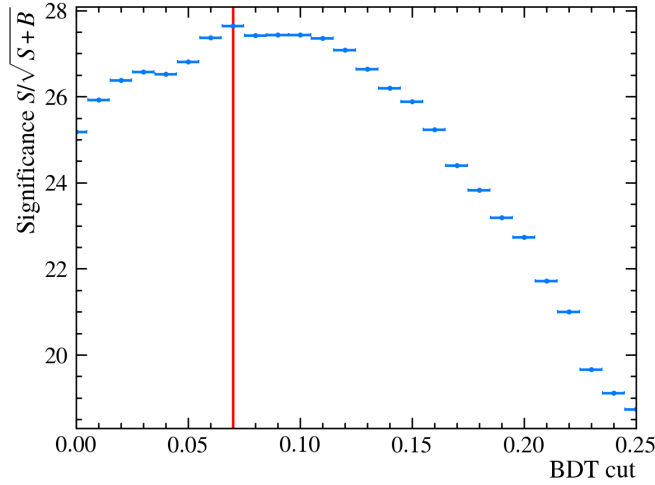


Figure 19: Dependence of the signal significance on the cut applied, for the BDT selector on Run2 Data. The red line indicates the optimal cut point ($BDT > 0.07$).

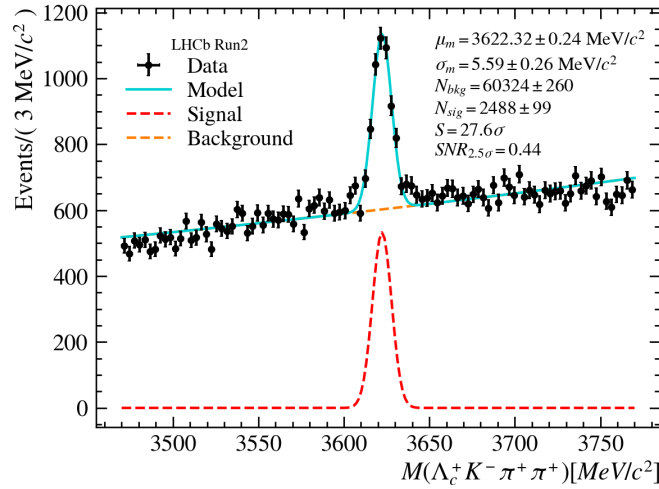


Figure 20: Fit to the invariant mass distribution for the Run2 Data around the mass peak.

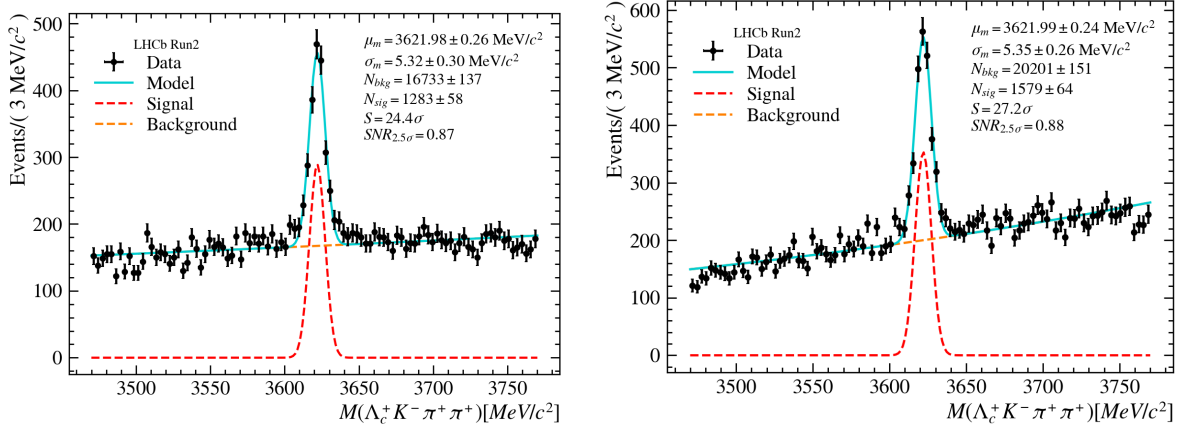


Figure 21: On the left, Ξ_{cc}^{++} mass distribution from our analysis with a tighter BDT cut ($BDT > 0.17$) to reduce the background level. On the right, Ξ_{cc}^{++} mass distribution from the mass measurement paper [16] using Run2 Data.

6 Search for excited doubly charmed baryons

6.1 Strategy

Our strategy to look for Ξ_{cc}^{++} excited states is to start from two different selections for Ξ_{cc}^{++} :

- Loose : more candidates but a lower signal purity
- Tight : less candidates but a higher signal purity

Then we are combining these candidates with a pion or kaon. At the end, we are performing 4 analyses (2 excited states \times 2 Ξ_{cc}^{++} selections).

6.2 MC simulation

In the simulation, pp collisions are generated under the same conditions as Sec. 4.1. The two excited baryons are required to have a $1 \text{ MeV}/c^2$ width³ which correspond to a lifetime of $6.58e-22\text{s}$. Moreover, for each baryon we have generated candidates with three different mass (see Tab. 11) and therefor six different EventType⁴.

Table 11: MC samples mass hypotheses.

Decay mode	EventType	Mass (MeV/c^2)
$\Xi_{cc}^{**+} \rightarrow \Xi_{cc}^{++}\pi^-$	26167051	3800.0
	26167052	3900.0
	26167053	4000.0
$\Omega_{cc}^{**+} \rightarrow \Xi_{cc}^{++}K^-$	26167054	4150.0
	26167055	4250.0
	26167056	4350.0

6.2.1 MC truth matching

The truth matching is done using true IDs, where we ask for each track to have the correct true ID and come from the true corresponding mother as :

$$\Xi_{cc}^+$$

```

abs(C_TRUEID)==4412&abs(Pi_TRUEID)==211&abs(Pi_MC_MOTHER_ID)==4412&
abs(Xicc_TRUEID)==4422&abs(Xicc_MC_MOTHER_ID)==4412&abs(Lc_TRUEID)==4122&
abs(LcP_TRUEID)==2212&abs(LcPi_TRUEID)==211&abs(LcK_TRUEID)==321&
(abs(LcP_MC_MOTHER_ID)==4122|abs(LcP_MC_GD_MOTHER_ID)==4122)&
(abs(LcK_MC_MOTHER_ID)==4122|abs(LcK_MC_GD_MOTHER_ID)==4122)&
(abs(LcPi_MC_MOTHER_ID)==4122|abs(LcPi_MC_GD_MOTHER_ID)==4122)&
abs(XiccPi1_TRUEID)==211&abs(XiccPi1_MC_MOTHER_ID)==4422&
abs(XiccPi1_MC_GD_MOTHER_ID)==4412&abs(XiccPi2_TRUEID)==211&

```

³Excited states have a narrower width than ground states

⁴Unique number to describe a decay and its simulation conditions

```

abs(XiccPi2_MC_MOTHER_ID)==4422&abs(XiccPi2_MC_GD_MOTHER_ID)==4412&
abs(XiccK_TRUEID)==321&abs(XiccK_MC_MOTHER_ID)==4422&
abs(XiccK_MC_GD_MOTHER_ID)==4412

 $\Omega_{cc}^+$ 

abs(C_TRUEID)==4432&abs(Pi_TRUEID)==321&abs(Pi_MC_MOTHER_ID)==4432&
abs(Xicc_TRUEID)==4422&abs(Xicc_MC_MOTHER_ID)==4432&abs(Lc_TRUEID)==4122&
abs(LcP_TRUEID)==2212&abs(LcPi_TRUEID)==211&abs(LcK_TRUEID)==321&
(abs(LcP_MC_MOTHER_ID)==4122|abs(LcP_MC_GD_MOTHER_ID)==4122)&
(abs(LcK_MC_MOTHER_ID)==4122|abs(LcK_MC_GD_MOTHER_ID)==4122)&
(abs(LcPi_MC_MOTHER_ID)==4122|abs(LcPi_MC_GD_MOTHER_ID)==4122)&
abs(XiccPi1_TRUEID)==211&abs(XiccPi1_MC_MOTHER_ID)==4422&
abs(XiccPi1_MC_GD_MOTHER_ID)==4432&abs(XiccPi2_TRUEID)==211&
abs(XiccPi2_MC_MOTHER_ID)==4422&abs(XiccPi2_MC_GD_MOTHER_ID)==4432&
abs(XiccK_TRUEID)==321&abs(XiccK_MC_MOTHER_ID)==4422&
abs(XiccK_MC_GD_MOTHER_ID)==4432

```

Finally, for both states, the number of events passing pre-selection and MC truth matching are reported in Tab. 12 and the invariant mass distributions are shown in Fig 22. We can see the three peaks for the different mass hypotheses.

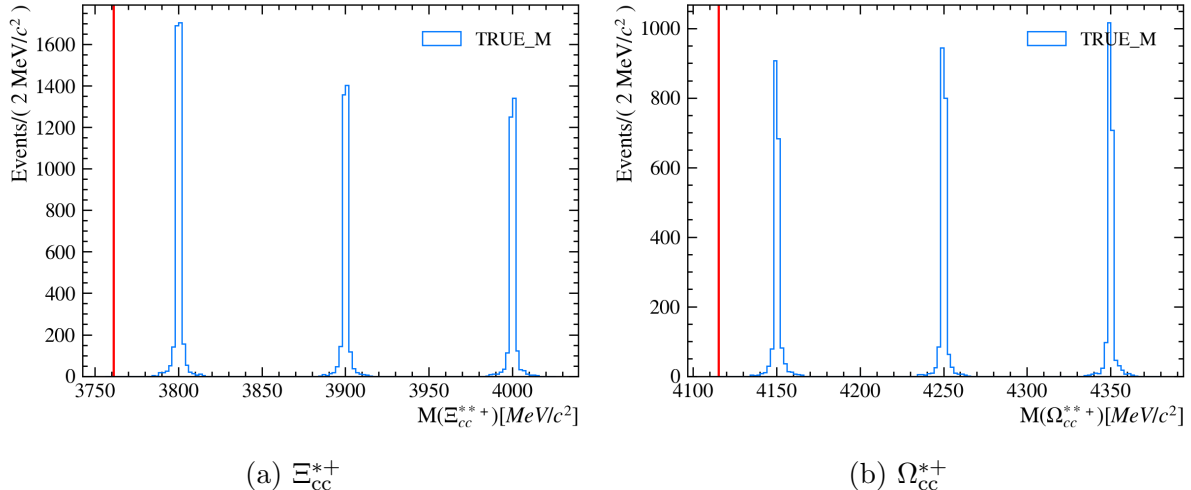


Figure 22: MC Truth signal Run2 used for training (Loose Ξ_{cc}^{++} cut).

Table 12: Total number of MC samples for both excited states (2016+2017+2018).

Ξ_{cc}^{++} Cut	Ξ_{cc}^{**+}	Ω_{cc}^{**+}
Loose	10115	5877
Tight	7216	4122

6.3 Selection

The $\Xi_{cc}^{**+} \rightarrow \Xi_{cc}^{++}\pi^-$ and $\Omega_{cc}^{**+} \rightarrow \Xi_{cc}^{++}K^-$ are selected with the following procedure.

- The Ξ_{cc}^{++} candidates are reconstructed following (see Sec. 5).
- A cut-based pre-selection is applied (see Sec. 6.3.1).
- A multivariate selection is applied (see Sec. 6.3.2).
- Clone and duplicated candidates are removed (see Sec. 6.3.3).

6.3.1 Offline reconstruction and pre-selection

The excited states candidates are reconstructed from the Ξ_{cc}^{++} candidates plus one track that pass appropriate hadron PID requirements, those cuts have been chosen in order to reduce the output file size while keeping as much signal candidates as possible. As well as having $p_T > 0.2 \text{ GeV}/c$, $\chi^2/ndf < 3$ and $\chi^2_{IP} < 16$ for K^- and π^- . The companion track and the Ξ_{cc}^{++} are required to form a vertex, and the fitted $\Xi_{cc}^{**+} / \Omega_{cc}^{**+}$ vertex must have $\chi^2_{vtx}/ndf < 25$. The selection for the excited states candidates is summarized in Tab. 13.

Table 13: Offline selection for the $\Xi_{cc}^{**+} \rightarrow \Xi_{cc}^{++}\pi^-$ and $\Omega_{cc}^{**+} \rightarrow \Xi_{cc}^{++}K^-$ decays.

Particles	Variable	Cuts
Ξ_{cc}^{++}	BDT	BDT>0.07 (Loose) or BDT>0.17 (Tight)
	Mass	$M \pm 15 \text{ MeV}/c^2$
π^- / K^-	Track quality	$\chi^2/ndf < 3$
	Impact parameter	$\chi^2_{IP} < 16$
	Transverse momentum	$p_T > 0.2 \text{ GeV}/c$
	π particle ID	$ProbNNpi > 0.1$
	K particle ID	$ProbNNk > 0.1$
$\Xi_{cc}^{**+} / \Omega_{cc}^{**+}$	Vertex quality	$\chi^2_{vtx}/ndf < 25$

6.3.2 Multivariate selection

The Run2 data and MC samples were used for the MVA training, and then applied a MVA cut to Run2 data. In the training, the simulated $\Xi_{cc}^{**+} \rightarrow \Xi_{cc}^{++}\pi^-$ and $\Omega_{cc}^{**+} \rightarrow \Xi_{cc}^{++}K^-$ events after the pre-selection and truth matching are used as signals, the WS samples ($\Xi_{cc}^{++}\pi^+$ and $\Xi_{cc}^{++}K^+$) and RS samples ($\Xi_{cc}^{++}\pi^-$ and $\Xi_{cc}^{++}K^-$) but with Ξ_{cc}^{++} sidebands candidates with the same pre-selection applied are used as backgrounds. The different Ξ_{cc}^{++} selections are shown in Fig. 23 where the width of the cuts have been choose to maximize the number of candidates for the training. Following a standard TMVA approach, both the signal and background samples were split randomly into two equally sized disjoint subsamples, one for the training and the other for the testing. Only the results for the Ξ_{cc}^{++} Looose selection are shown below, the ones for Tight selection are shown in Appendix C. For all different types of training will use the 5 variables listed in Tab. 14. Their distributions are shown in Fig. 24,29. Their correlation matrices are shown in Fig. 25,30. The boosted decision tree (BDT and BDTG) based and the multilayer perceptron (MLP)

based selectors were considered to give the best performance according to the previous analysis. The Receiver Operating Characteristic (ROC) curves of these three selectors are shown in Fig. 26,31, and the MVA output distributions are shown in Fig. 27,32. Here the working point is determined by maximizing the so-called Punzi Figure of Merit (FoM) defined as :

$$FoM_{Punzi} = \frac{\epsilon_{sig}}{a/2 + \sqrt{B}} \quad (4)$$

where :

- ϵ_{sig} is the efficiency of the cuts on the signal.
- a is the desired significance.
- B is the expected number of background candidates.

The Punzi Figures of Merit are shown for different selectors in Fig. 28,33. The blue line shows the best cut among the three selectors, which have been applied for the following steps. The three selectors give similar performances but the MLP one have the best results overall. Here we were using a different function because the states we were looking for were not yet discovered.

Table 14: The 5 variables used in MVA selectors.

1.	$\log(\chi^2_{IP})$ of $\Xi_{cc}^{**+}/\Omega_{cc}^{**+}$ to its PV
2.	Transverse momentum p_T of $\Xi_{cc}^{**+}/\Omega_{cc}^{**+}$
3.	$\log(\chi^2_{IP})$ of π^-/\bar{K}^-
4.	ProbNNpi/k of π^-/\bar{K}^-
5.	Transverse momentum p_T of π^-/\bar{K}^-

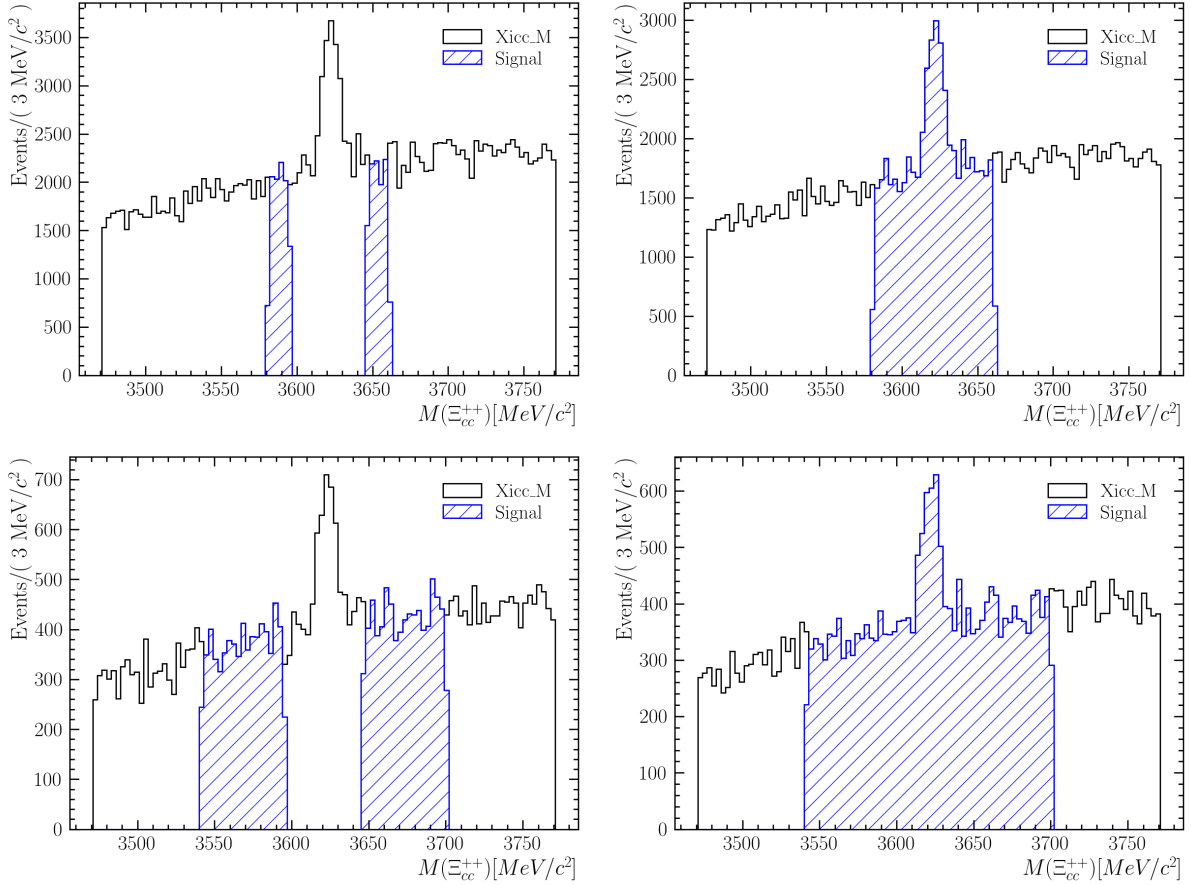


Figure 23: Ξ_{cc}^{++} selection for the RS samples (on the left) using upper and lower sidebands starting $25 \text{ MeV}/c^2$ away from the mean value and for the WS samples (on the right). The selection is larger ($\pm 80 \text{ MeV}/c^2$ vs $\pm 40 \text{ MeV}/c^2$) for Ω_{cc}^+ (on the bottom) due to the lower statistic than the selection Ξ_{cc}^+ (on the top).

Ξ_c^+ Results :

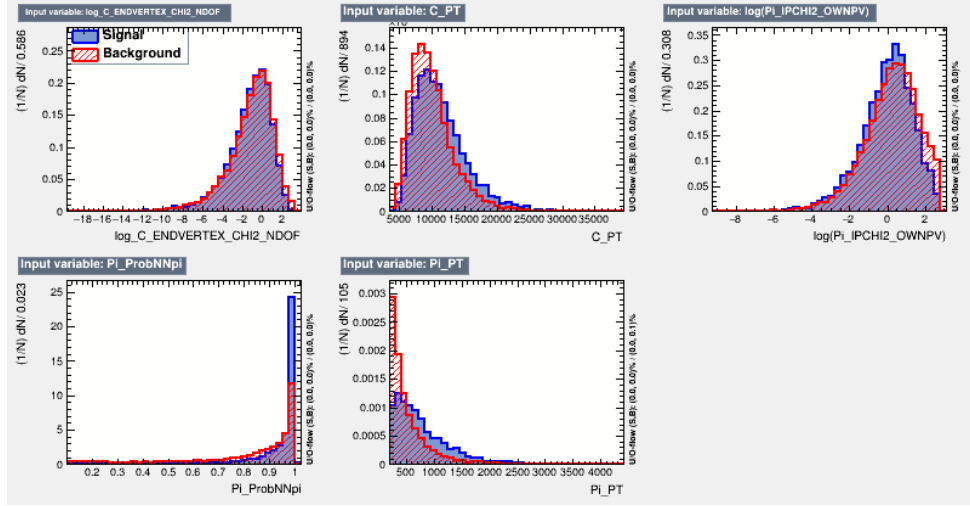


Figure 24: Distributions of input variables, compared between (blue) signals and (red) backgrounds.

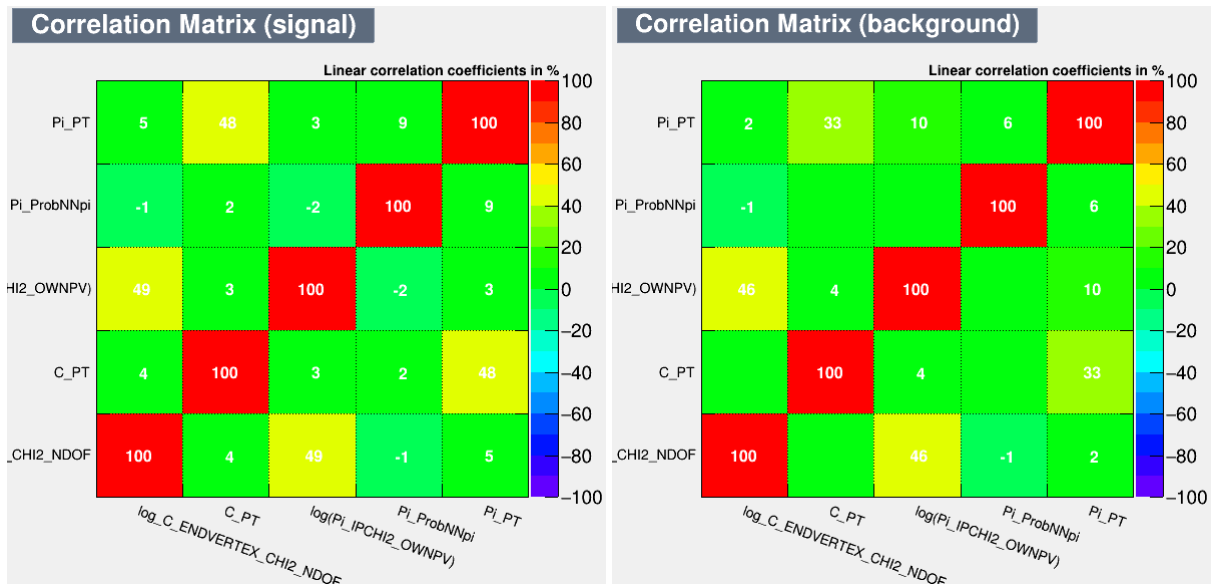


Figure 25: Correlation matrices for the 5 variables used in the multivariate selector, for (left) signal and (right) background.

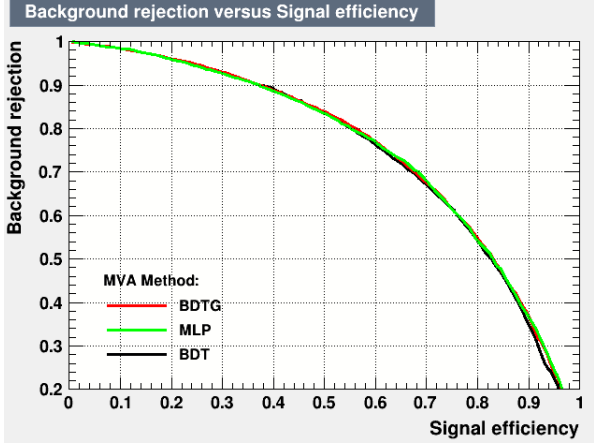


Figure 26: ROC curves for MVA selectors. The vertical axis shows the background rejection fraction, and the horizontal the signal efficiency.

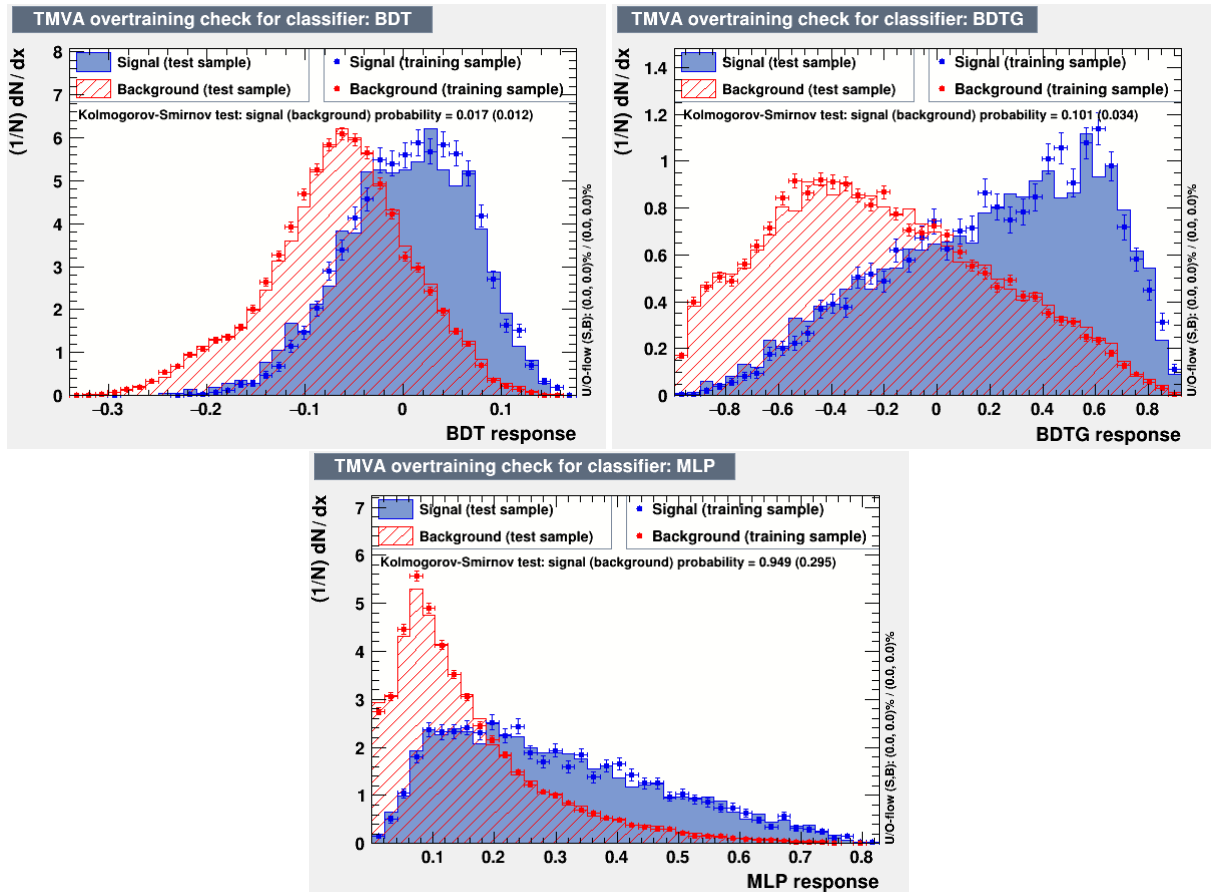


Figure 27: Response curves for MVA selectors: (top left) BDT, (top right) BDTG, (bottom) MLP. For each plot, the horizontal axis shows the MVA output and the vertical axis shows the normalised distribution. The output for the training sample is shown as points with error bars and the output for the test sample is shown as a shaded/hatched histogram.

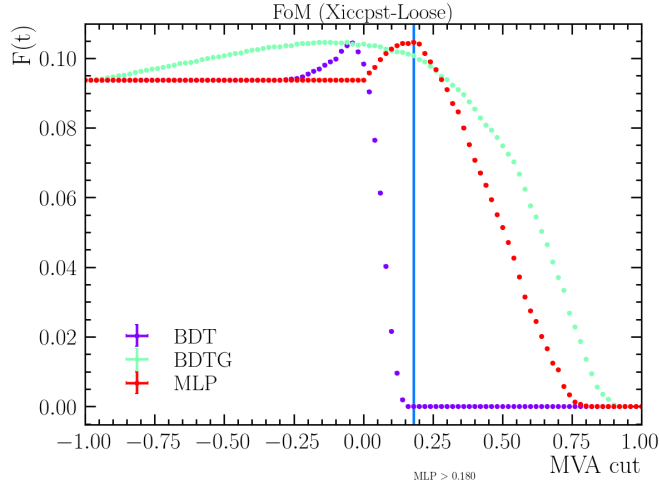


Figure 28: Dependence of the signal significance on the cut applied, for three different selectors.

Ω_{cc}^+ Results :

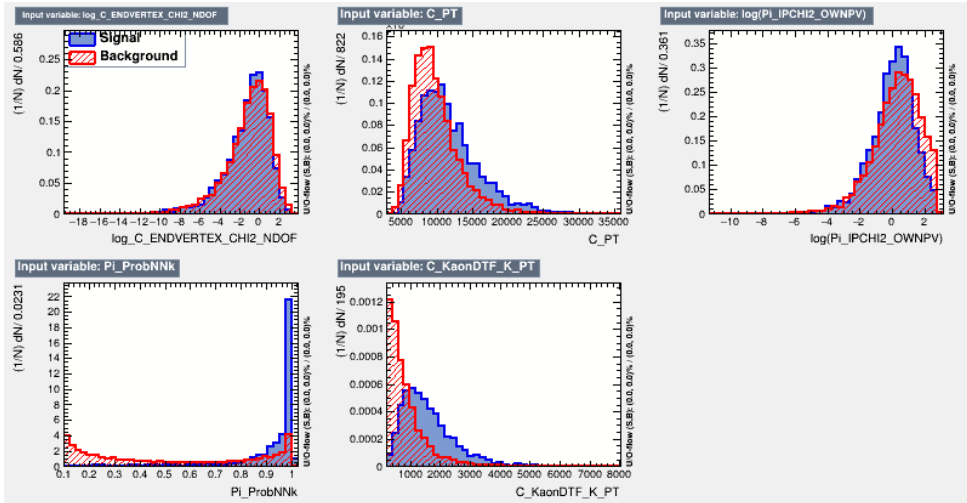


Figure 29: Distributions of input variables, compared between (blue) signals and (red) backgrounds.

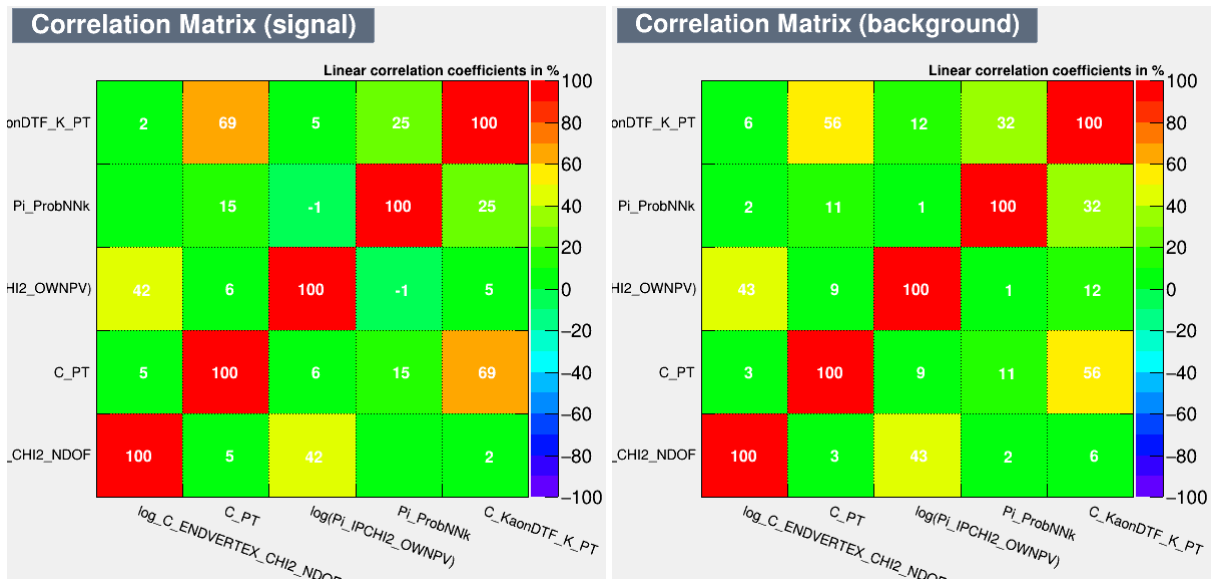


Figure 30: Correlation matrices for the 5 variables used in the multivariate selector, for (left) signal and (right) background.

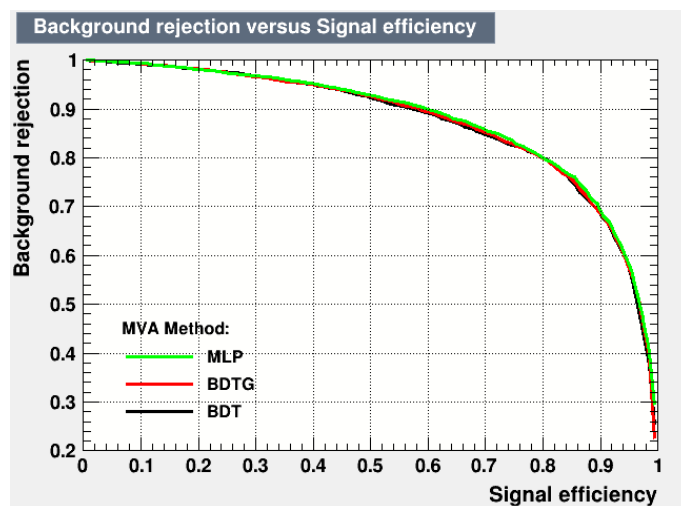


Figure 31: ROC curves for MVA selectors. The vertical axis shows the background rejection fraction, and the horizontal the signal efficiency.

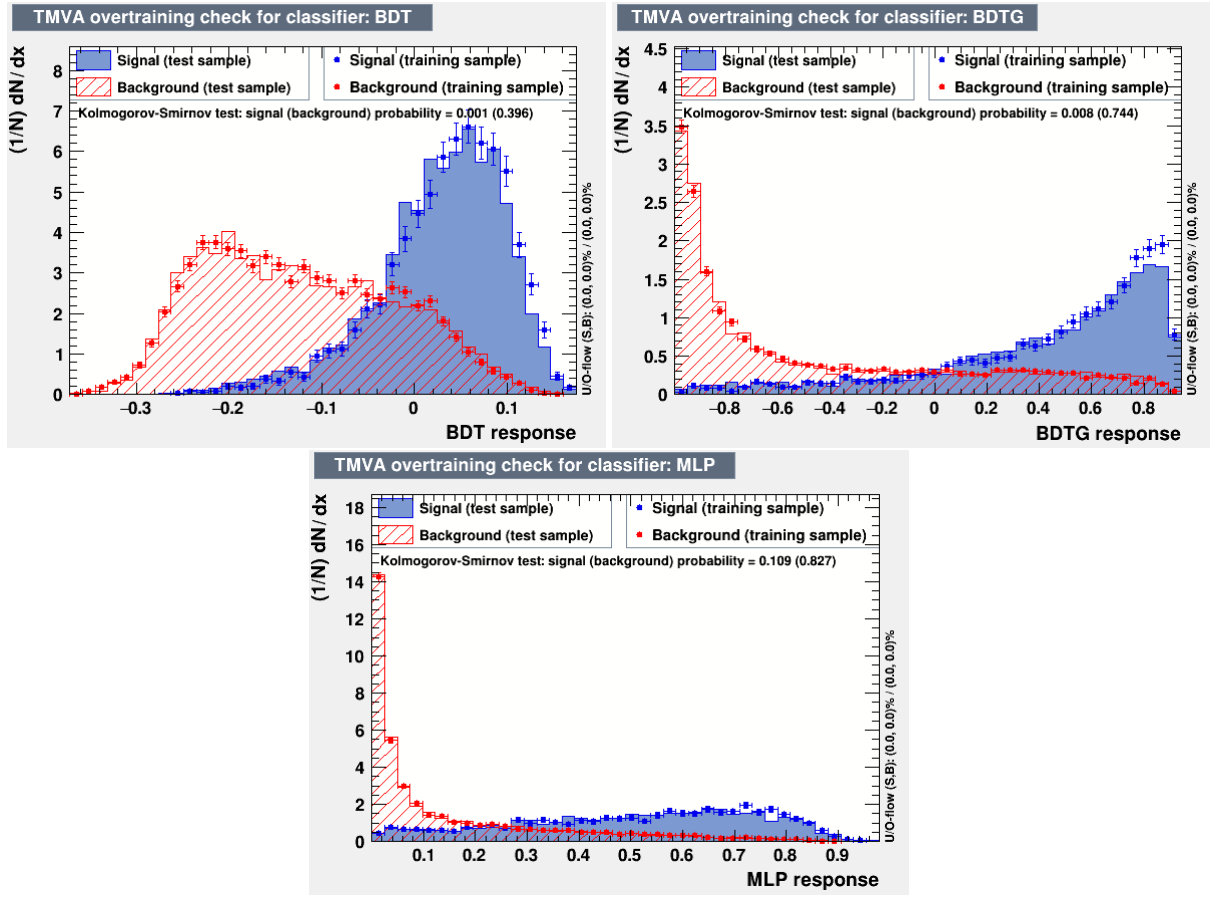


Figure 32: Response curves for MVA selectors: (top left) BDT, (top right) BDTG, (bottom) MLP. For each plot, the horizontal axis shows the MVA output and the vertical axis shows the normalised distribution. The output for the training sample is shown as points with error bars and the output for the test sample is shown as a shaded/hatched histogram.

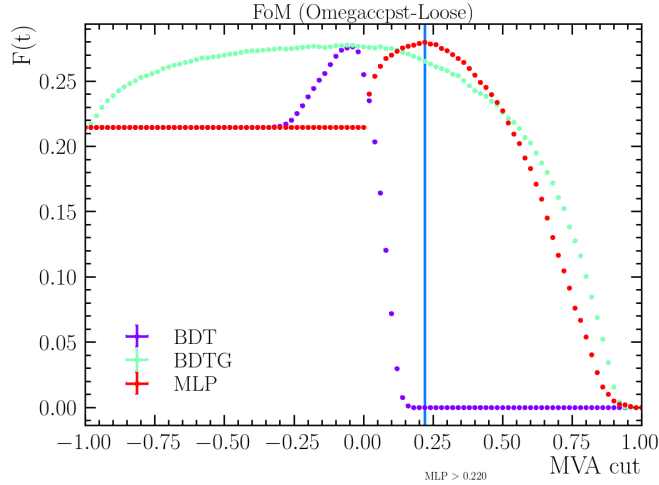


Figure 33: Dependence of the signal significance on the cut applied, for three different selectors.

6.3.3 Removal of internal track clone candidates and duplicated candidates

The method is exactly the same as in Sec. 5.2.4 except that now it's using 7 tracks (6 previous tracks and the additional companion track) to check for internal track clone candidates and duplicated candidates. Tab. 15,16 show the number of removed duplicated candidates who shares all seven tracks. In 2016, there is still a high number of removed candidates due to the same issue.

Year	Yields before removal	Removed clone	Removed duplication	Yields after removal
2016	10901	-16 (-0.15%)	-4430 (-40.70%)	6455 (59.21%)
2017	3652	-3 (-0.08%)	-158 (-4.33%)	3491 (95.59%)
2018	8748	-15 (-0.17%)	-491 (-5.62%)	8242 (94.22%)

Table 15: Yields and number of removed clone and duplicated candidates in 2016-2018 data (Xiccp-RS-Loose, Xiccpp 15 MeV/c² mass window, 500 MeV/c² mass window).

Year	Yields before removal	Removed clone	Removed duplication	Yields after removal
2016	1882	-9 (-0.76%)	-811 (-43.30%)	1062 (56.43%)
2017	592	-1 (-0.17%)	-48 (-8.12%)	543 (91.72%)
2018	1486	-6 (-0.40%)	-112 (-7.57%)	1368 (92.06%)

Table 16: Yields and number of removed clone and duplicated candidates in 2016-2018 data (Omegaccp-Loose).

6.4 Mass fit

The mass fit was again achieved by summing two models, one describing the signal distribution and the other the background distribution. In this section, we used different

models than before. Indeed, here we want the most accurate model possible, so for the signal we've used a modified Gaussian function with power-law tails on both sides named the Double Sided Crystal Ball which is described below. Finally, given the different distribution of the background noise, we had to find a suitable model.

6.4.1 MC mass fit

To find out the expected signal distribution, we used simulation data to determine the model to be used and the parameters. The Double Sided Crystal Ball described in Eq. 5,6 have shown the best result on MC data (see Fig. 34).

For the final fit, only the mean value is left free and all other parameters are fixed with the values obtained at this stage. These parameters are shown in the top-right corner of the plots in Fig. 34.

Double Sided Crystal Ball

$$f(x; \mu, \sigma, \alpha_L, n_L, \alpha_R, n_R) = \begin{cases} A_L \cdot (B_L - \frac{x-\mu}{\sigma})^{-n_L}, & \text{for } \frac{x-\mu}{\sigma} < -\alpha_L \\ \exp(-\frac{(x-\mu)^2}{2\sigma^2}), & -\alpha_L \leq \frac{x-\mu}{\sigma} \leq \alpha_R \\ A_R \cdot (B_R - \frac{x-\mu}{\sigma})^{-n_R}, & \text{for } \frac{x-\mu}{\sigma} > \alpha_R \end{cases} \quad (5)$$

with

$$\begin{aligned} A_{L/R} &= \left(\frac{n_{L/R}}{|\alpha_{L/R}|} \right)^{n_{L/R}} \cdot \exp \left(-\frac{|\alpha_{L/R}|^2}{2} \right) \\ B_{L/R} &= \frac{n_{L/R}}{|\alpha_{L/R}|} - |\alpha_{L/R}| \end{aligned} \quad (6)$$

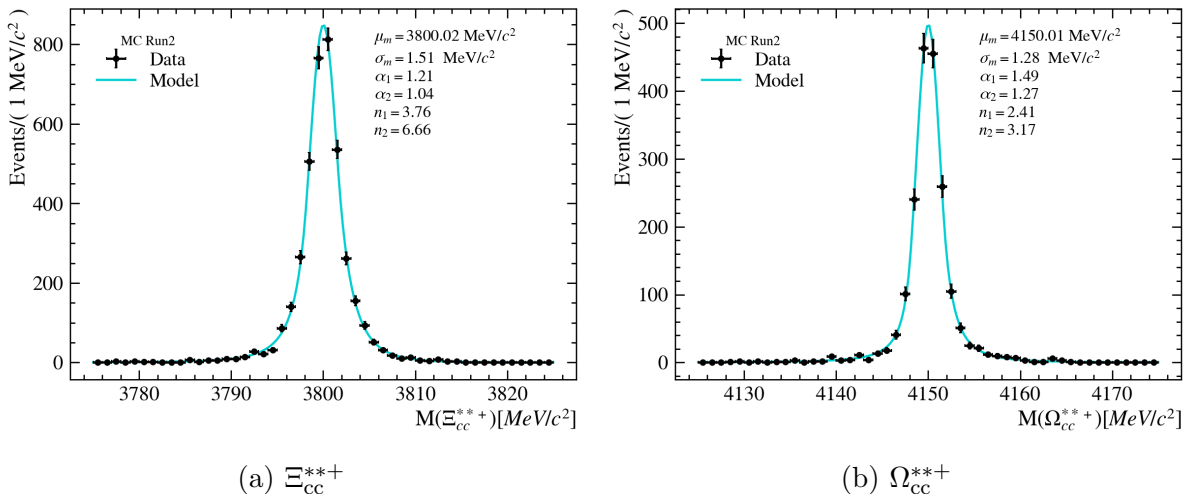


Figure 34: Signal model fit on MC samples.

6.4.2 Background fit

To find out the expected background distribution, we used Wrong Sign data to determine the model to be used and the parameters. There was no simple function to fit the distribution, so a custom model had to be determined. It is described in Eq. 7 and the fitting results on WS data are shown in Fig. 35).

Custom pdf

$$f(\Delta M; a, b) = \Delta M^a \times \exp(-b \cdot \Delta M) \quad (7)$$

where :

$$\begin{aligned} \Delta M &= m(\Omega_{cc}^+) - m(\Xi_{cc}^{++}) - m(K^-) \\ &\text{or} \\ \Delta M &= m(\Xi_{cc}^+) - m(\Xi_{cc}^{++}) - m(\pi^-) \end{aligned} \quad (8)$$

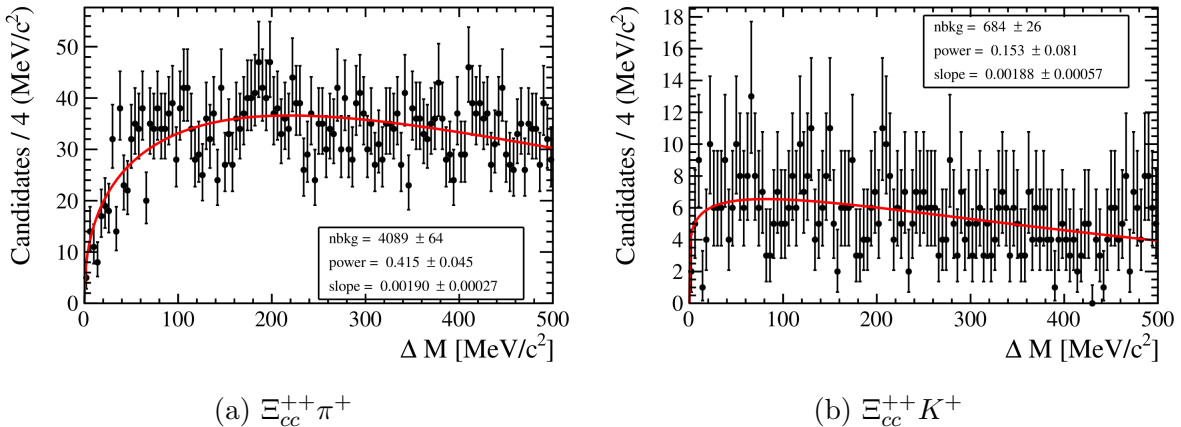


Figure 35: Background model fit on WS samples.

6.5 Mass distributions and signal significance

The mass distribution of the different samples for each analysis after all selections applied is shown in Fig. 36. The mass distribution for RS, WS and SB samples match well except for the SB sample for the Ξ_{cc}^+ Tight selection due to a missing cut. Moreover, we can see a small peak for the Ω_{cc}^+ Loose selection but no significant structure is observed through the different analyses. The local significance of the signal peak is quantified with a p-value, which is calculated below.

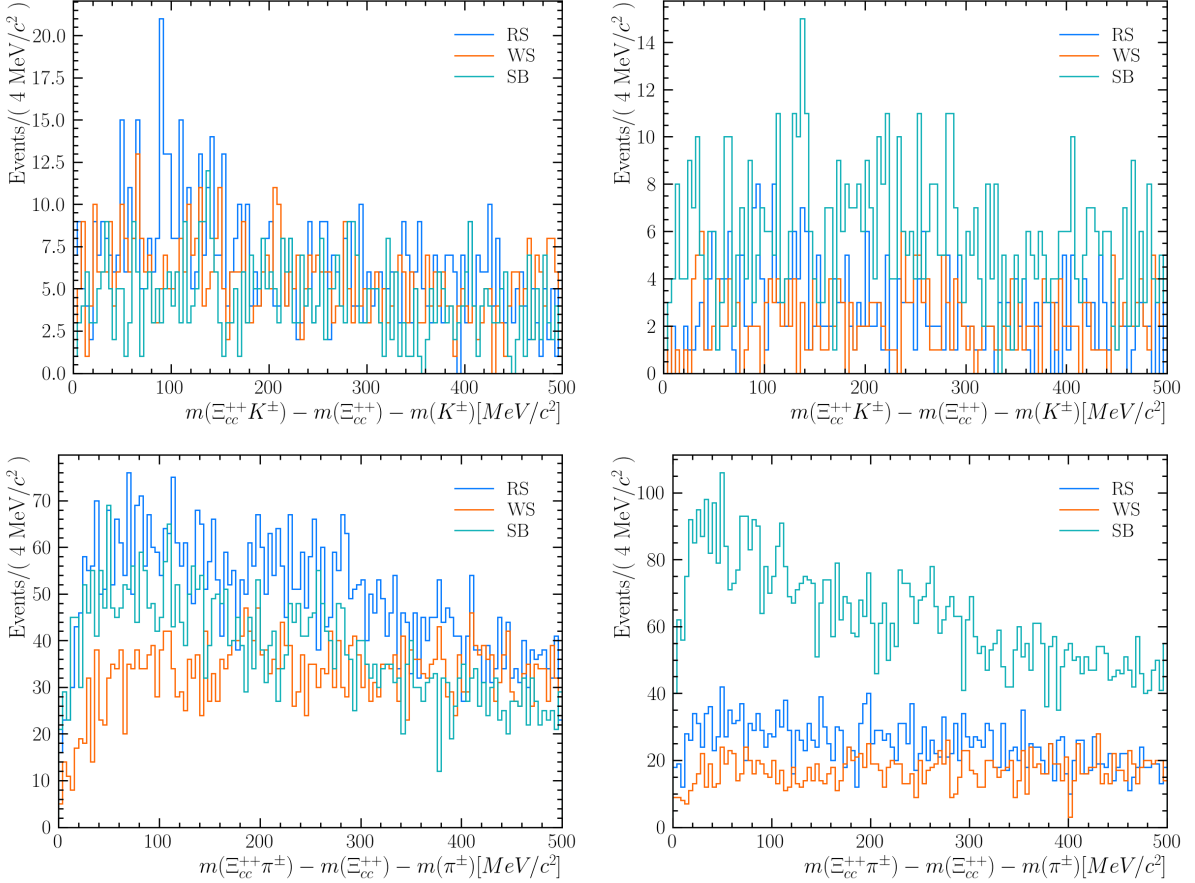


Figure 36: Mass distributions of RS, WS and SB samples for each analysis. Ω_{cc}^+ Loose selection (top left), Ω_{cc}^+ Tight selection (top right), Ξ_{cc}^+ Loose selection (bottom left) and Ξ_{cc}^+ Tight selection (bottom right).

The local p -value is determined as a function of the mass in steps of $1 \text{ MeV}/c^2$. The p -values are determined from the test statistics q_{\pm} (see Eq. 12), which are based on the ratio of likelihoods of the fit under the background-only (H_0 i.e. $\mu = 0$ in Eq. 9) and signal-plus-background hypotheses (H_1 i.e. $\mu \neq 0$). The q -values can be simplified using the Negative Log-Likelihood (NLL) loss function after fitting (see Eq. 10). The test statistics are defined similarly to the test statistic q_0 defined in Ref. [27], but contrary to q_0 the test statistic q_{\pm} is assigned the value $-q_0$ when the fit yields a negative number of signal candidates (see Eq. 11), in order to obtain a smooth p -value curve also for downward fluctuations.

$$N_{tot} = N_{bkg} + \mu N_{sig} \quad (9)$$

$$q_0 = -2 \ln \left(\frac{L(0, \theta)}{L(\hat{\mu}, \hat{\theta})} \right) = 2(\text{NLL}(H_0) - \text{NLL}(H_1)) \quad (10)$$

$$q\text{-value} = \begin{cases} q_0, & \hat{\mu} > 0 \\ -q_0, & \hat{\mu} < 0 \end{cases} \quad (11)$$

$$p\text{-value} = \frac{1 - \text{erf}(\sqrt{q\text{-value}/2})}{2} \quad (12)$$

The local p-value is plotted in Fig. 37 and Fig. 39 a function of the mass difference, ΔM . The global significance have not been evaluated but it takes into account the look-elsewhere effect which reduces the significance. The results of the p-value scans and the corresponding fitting using the Ξ_{cc}^{++} loose selection are shown below Fig. 38 and Fig. 40. The number of events is too low using the tight selection to get significant results.

The Ω_{cc}^{*+} state shows a dip around $\Delta M = 93 \text{ MeV}/c^2$, which has the largest local significance, corresponding to 3.8 standard deviations. And the Ξ_{cc}^{*+} state shows a dip around $\Delta M = 34 \text{ MeV}/c^2$, which has the largest local significance, corresponding to 2.9 standard deviations.

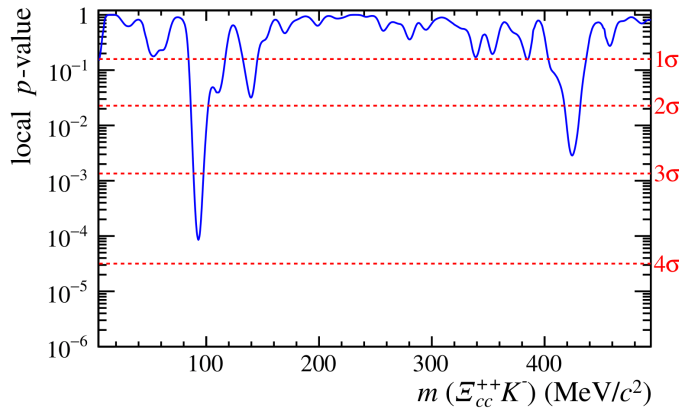


Figure 37: (Color online) Local p-value of selected Ω_{cc}^{*+} candidates at different ΔM values evaluated with the likelihood ratio test. Lines indicating one, two, three and four standard deviations (σ) of local significance are also shown.

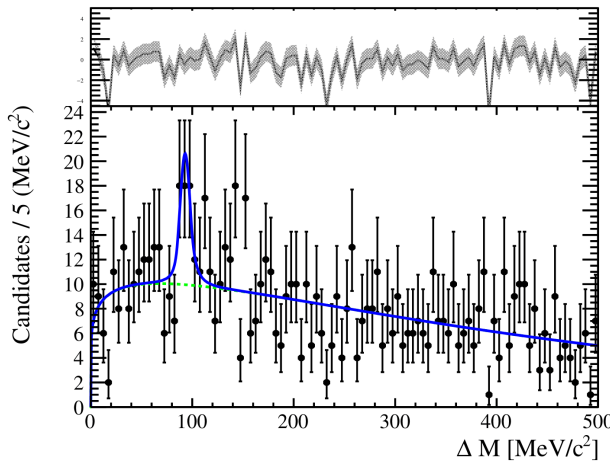


Figure 38: Distribution of selected Ω_{cc}^{*+} candidates (black points). The fit results for $\Delta M = 93 \text{ MeV}/c^2$ are superimposed.

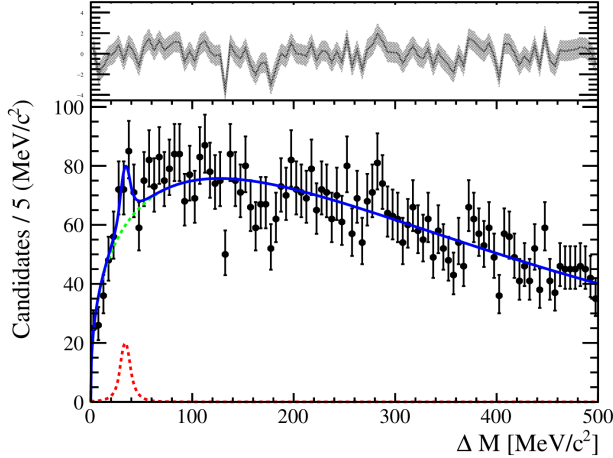


Figure 40: Distribution of selected Ξ_{cc}^{*+} candidates (black points). The fit results for $\Delta M = 34 \text{ MeV}/c^2$ are superimposed.

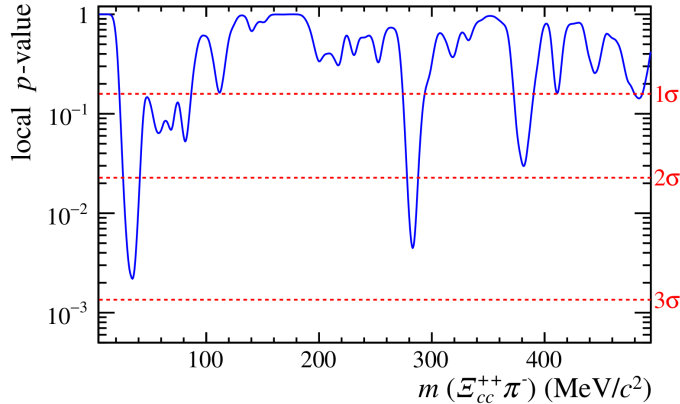


Figure 39: (Color online) Local p -value of selected Ξ_{cc}^{*+} candidates at different ΔM values evaluated with the likelihood ratio test. Lines indicating one, two and three standard deviations (σ) of local significance are also shown.

7 Conclusion

A search for both the Ξ_{cc}^{*+} baryon through the $\Xi_{cc}^{*+}\pi^-$ decay and the Ω_{cc}^{*+} baryon through the $\Xi_{cc}^{*+}K^-$ decay are performed, using pp collision data collected by the LHCb experiment from 2016 to 2018 at a centre-of-mass energy of 13 TeV, corresponding to an integrated luminosity of 5.4 fb^{-1} . No significant signal is observed in the mass range of 0 to 500 MeV/c^2 from the mass threshold. Future searches by the LHCb experiment with upgraded detectors, improved trigger conditions, additional Ξ_{cc}^{*+} and Ω_{cc}^{*+} decay modes, and larger data samples will further increase Ξ_{cc}^{*+} and Ω_{cc}^{*+} signal sensitivity.

Appendices

Appendix A Introduction of the detector

The LHCb experiment is situated at one of the four points around CERN’s Large Hadron Collider where beams of protons are smashed together, producing an array of different particles.

The aim of the LHCb experiment is to record the decay of particles containing b and anti-b quarks, collectively known as ‘B mesons’. The experiment’s 4,500 tonne detector (see Fig. 41) is specifically designed to filter out these particles and the products of their decay [28, 29].

Rather than flying out in all directions, B mesons formed by the colliding proton beams (and the particles they decay into) stay close to the line of the beam pipe, and this is reflected in the design of the detector. Other LHC experiments surround the entire collision point with layers of sub-detectors, like an onion, but the LHCb detector stretches for 20 metres along the beam pipe, with its sub-detectors stacked behind each other like books on a shelf.

The detector aims to measure production and decay properties of heavy flavour hadrons. These hadrons have a short lifetime therefore the measurements are hard to be performed directly on them. Instead it’s easier to use stable particles such as protons, electrons, muons etc. which can fly over long distances.

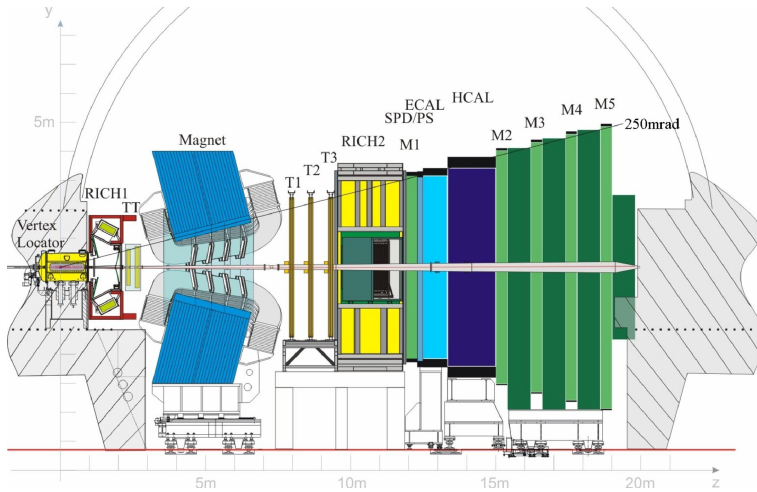


Figure 41: LHCb detector.

A.1 Sub-detectors

Each one of LHCb’s sub-detectors specializes in measuring a different characteristic of the particles produced by colliding protons.

VELO The Vertex Locator is built around the proton interaction region. It is used to measure the particle trajectories close to the interaction point in order to precisely

separate primary and secondary vertices.

RICH-1 The first Ring imaging Cherenkov detector is located directly after the vertex detector. It is used for particle identification of low-momentum tracks.

TT,T1/T2/T3 The main tracking system is placed before (TT) and after (T1/T2/T3) the dipole magnet. It is used to reconstruct the trajectories of charged particles and to measure their momenta.

RICH-2 The second Ring imaging Cherenkov detector follows the tracking system. It allows the identification of the particle type of high-momentum tracks.

HCAL/ECAL The electromagnetic and hadronic calorimeters provide measurements of the energy of electrons, photons, and hadrons. These measurements are used at trigger level to identify the particles with large transverse momentum (high-Pt particles).

M1-M5 The muon system is used to identify and trigger on muons in the events.

A.2 Trigger levels

The LHC can provide a bunch crossing every 25ns that leads to a data rate of 40MHz but it's impossible to save 1TB/s because the FPGA maximal readout is 1MHz and the maximal storage rate is 12.5kHz. In order to reduce the storage rate the detector have to select only relevant events. This is made possible by the three trigger levels [30, 31] (see Fig. 42).

L0 Trigger The L0 trigger reconstructs and selects particles with high transverse momentum in the muon chambers or with high transverse energy in the calorimeter system. The purpose of the L0 trigger is to reduce the rate to 1.1 MHz

HLT1 Trigger The first High Level Trigger reduces the rate from the 1.1 MHz output of the L0 trigger to a few tens of kHz. It applies different sequences of algorithms. The strategy is to confirm the Level-0 candidates by adding information from either the VELO or the main tracker and applying cuts on the transverse momentum (p_T) and the impact parameter (IP) with respect to the primary vertex.

HLT2 Trigger The HLT second level performs a full pattern recognition on the remaining events by adding RICH information (Particle Identification). On the fully reconstructed events, a combination of inclusive selection of specific resonances (such as J/ψ or D^*) and exclusive reconstruction of B-hadron final states is performed. The final trigger decision is an OR between the inclusive and exclusive selections.

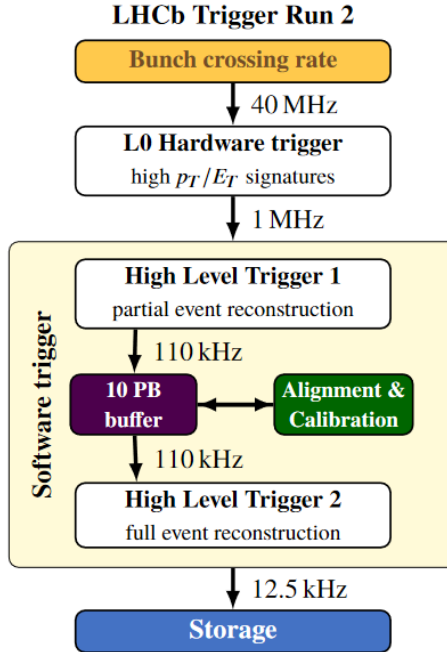


Figure 42: Overview of the LHCb trigger system.

A.3 Dataflow

All events with a positive trigger decision are saved on disk on DST files that are suitable for analysis. To save disk space and to speed up access for analysts, the tracks saved for an event can be reduced to signal only, these are the exclusive lines (Fig. 3a) which save only tracks relevant to reconstruct the decay we want. In contrast, inclusive lines (Fig. 3b) save other tracks since some calculations need them. Moreover, the output files are grouped into streams which contain similar selections. By grouping all of the fully hadronic charm selections together, for example, analysts interested in that type of physics don't waste time running over the output of the dimuon selections.

Then, users can run their own analysis tools to extract variables for their analysis with the DaVinci application. With a Python script users specify which data they want to process and which decays they want to reconstruct. Because there is a lot of data it's necessary to apply cut selection to reduce the size of the ROOT output file called ntuple. Finally, the ntuples are processed locally to apply further selection as a MVA selector [32].

We also produced lots of simulated events, often called Monte Carlo data, and this is processed in a very similar way to real data. This similarity is very beneficial, as the simulated data is subject to the same deficiencies as in the processing of real data. The MC data can be used to train a MVA selector.

Appendix B Sanity checks

B.1 Polarity

The number of candidates in the MagnetDown dataset is slightly lower as shown in Tab. 17 and Fig. 43. This difference can be explained by the difference of luminosity between the two datasets mentioned in Sec. 4.2.2.

Table 17: The signal yield, mean value and mass resolution depending of the polarity.

Magnet	Signal yield	Mean value μ	Mass resolution σ
Up	263 ± 32	3621.24 ± 0.85	6.59 ± 1.0
Down	221 ± 32	3622.45 ± 1.0	6.78 ± 1.3

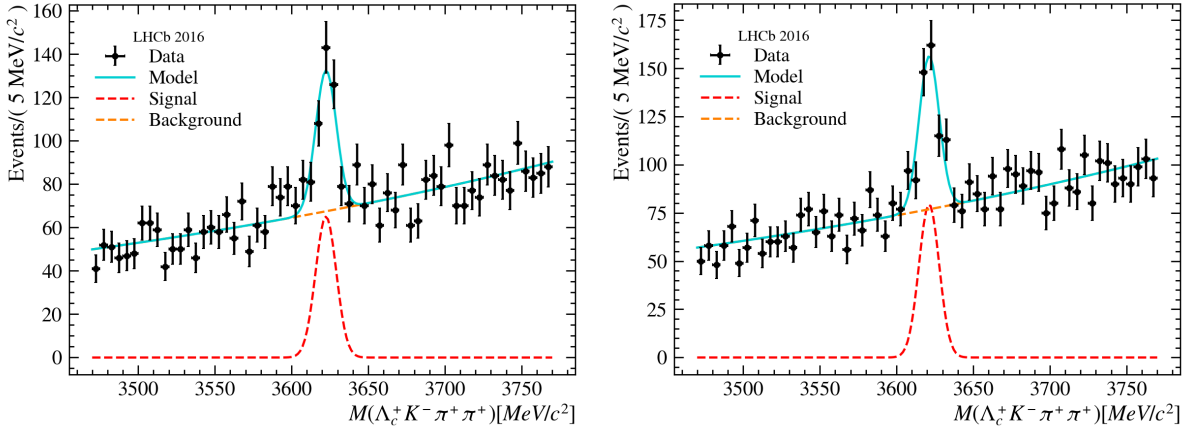


Figure 43: The fit results of (left) MagUp data and (right) MagDown data.

B.2 Charge conjugations

The difference of yield between Ξ_{cc}^{--} and Ξ_{cc}^{++} showed in Tab. 18 and Fig. 44 have already been mention by the mass measurement analysis as a potential CP violation.

Table 18: The signal yield, mean value and mass resolution depending of the charge conjugation.

Ξ_{cc}	Signal yield	Mean value μ	Mass resolution σ
Ξ_{cc}^{++}	198 ± 28	3622.17 ± 0.84	5.60 ± 1.0
Ξ_{cc}^{--}	291 ± 33	3621.21 ± 0.96	7.77 ± 1.0

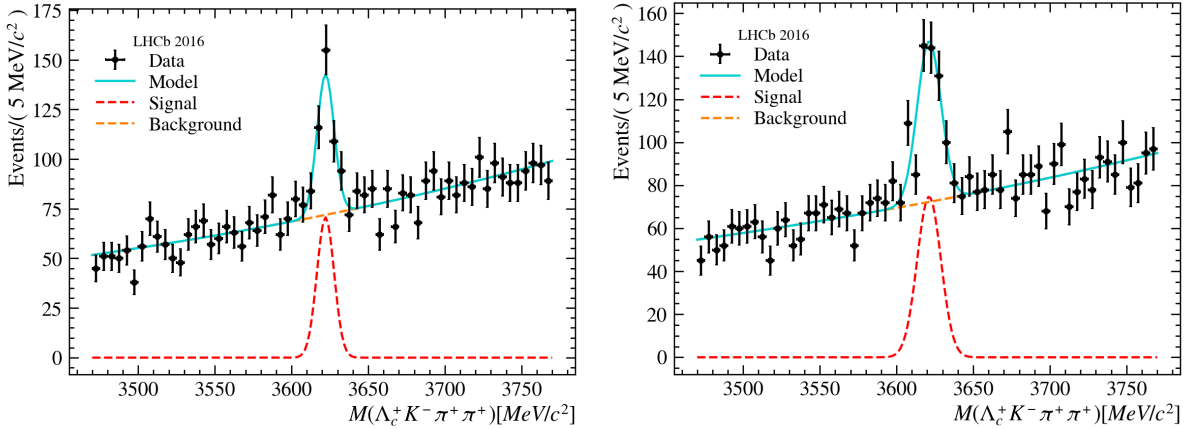


Figure 44: The fit results of (left) Ξ_{cc}^{++} and (right) $\bar{\Xi}_{cc}^{--}$.

B.3 Λ_c^+ signal vs sidebands

The Λ_c^+ signal window defined as $[2270, 2306]$ MeV/ c^2 and the Λ_c^+ sideband regions defined as $[2222, 2258] \cup [2318, 2354]$ MeV/ c^2 , are shown in Fig. 45.

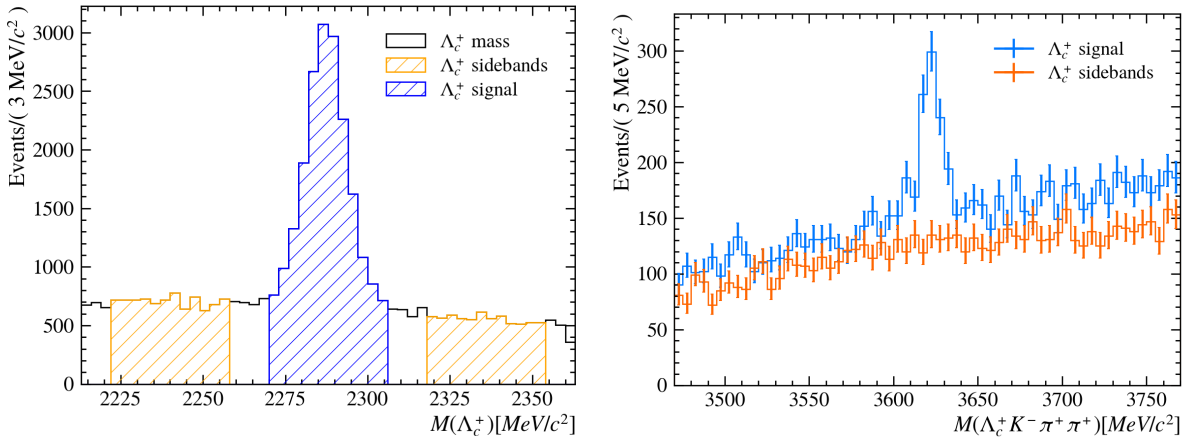


Figure 45: On the left, Λ_c^+ invariant mass distribution, with shaded area indicating (blue) the signal region and (orange) the sideband regions. Events are taken from the Data sample with MVA cuts applied. On the right, Ξ_{cc}^{++} invariant mass distribution using the Λ_c^+ signal region in blue and the sideband region in orange.

Appendix C MVA training results with Ξ_{cc}^{++} Tight selection

Ξ_{cc}^{+} Results :

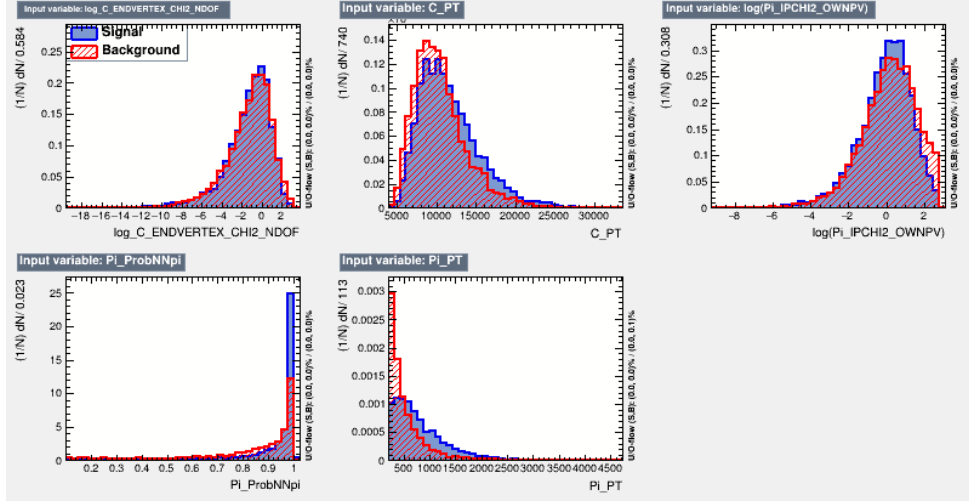


Figure 46: Distributions of input variables, compared between (blue) signals and (red) backgrounds.

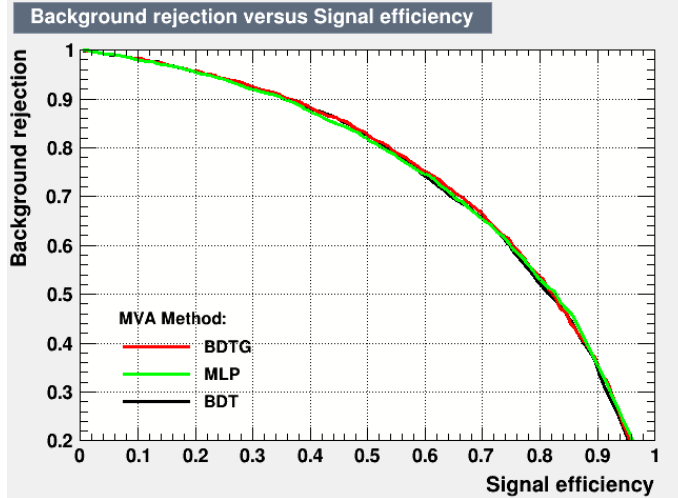


Figure 47: ROC curves for MVA selectors. The vertical axis shows the background rejection fraction, and the horizontal the signal efficiency.

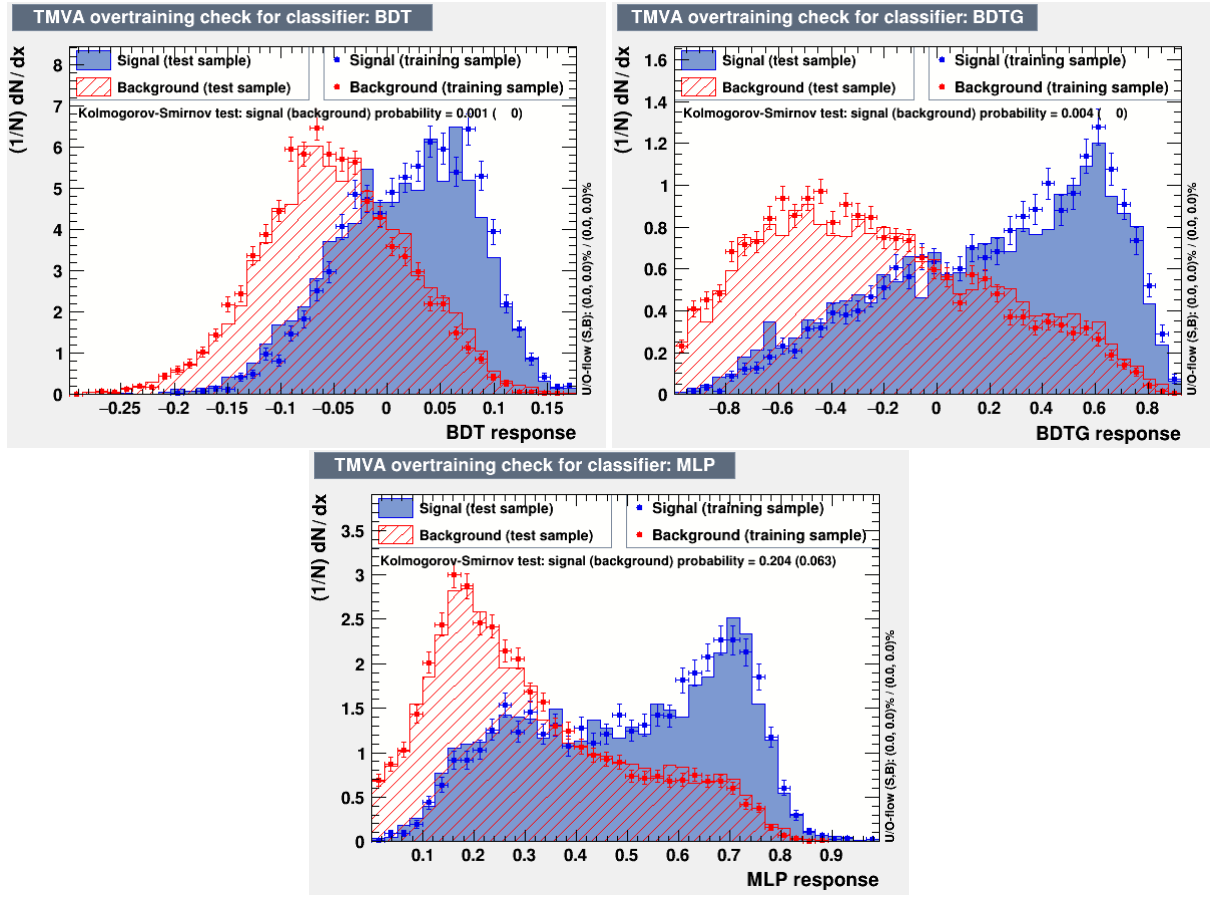


Figure 48: Response curves for MVA selectors: (top left) BDT, (top right) BDTG, (bottom) MLP. For each plot, the horizontal axis shows the MVA output and the vertical axis shows the normalised distribution. The output for the training sample is shown as points with error bars and the output for the test sample is shown as a shaded/hatched histogram.

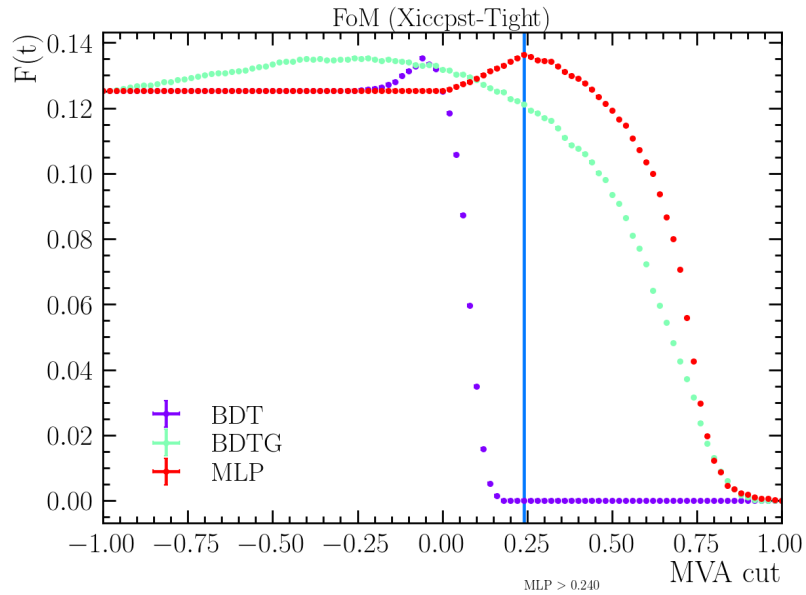


Figure 49: Dependence of the signal significance on the cut applied, for three different selectors.

Ω_{cc}^+ Results :

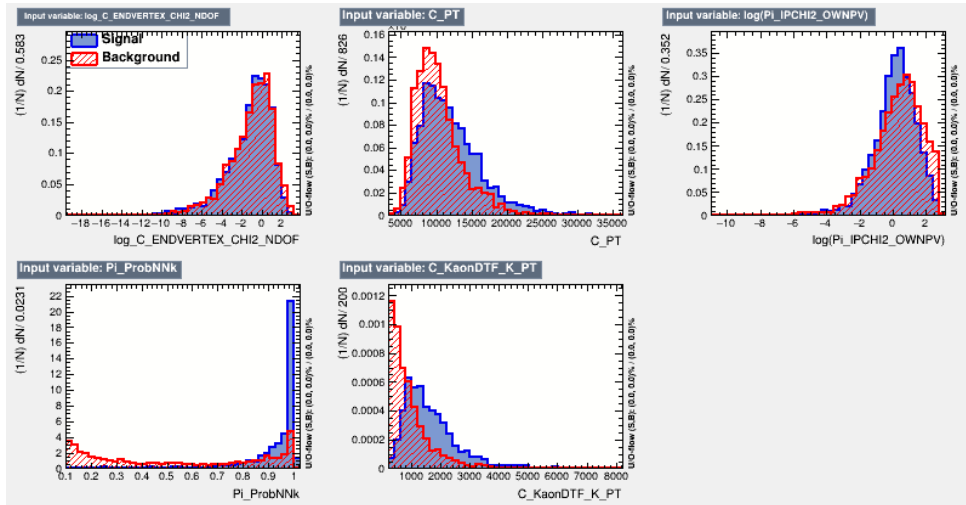


Figure 50: Distributions of input variables, compared between (blue) signals and (red) backgrounds.

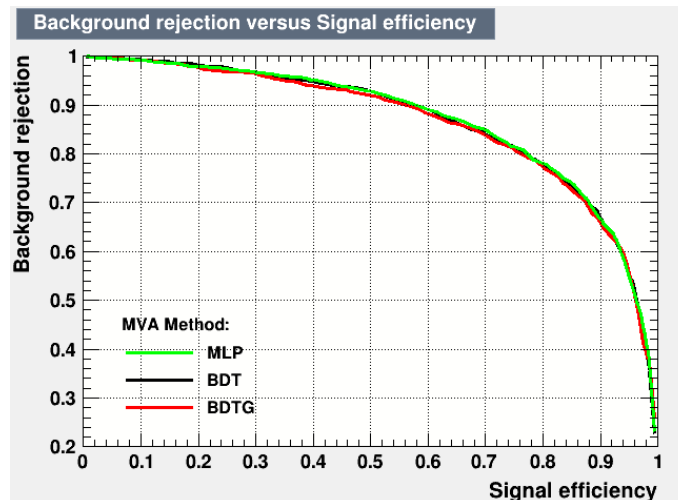


Figure 51: ROC curves for MVA selectors. The vertical axis shows the background rejection fraction, and the horizontal the signal efficiency.

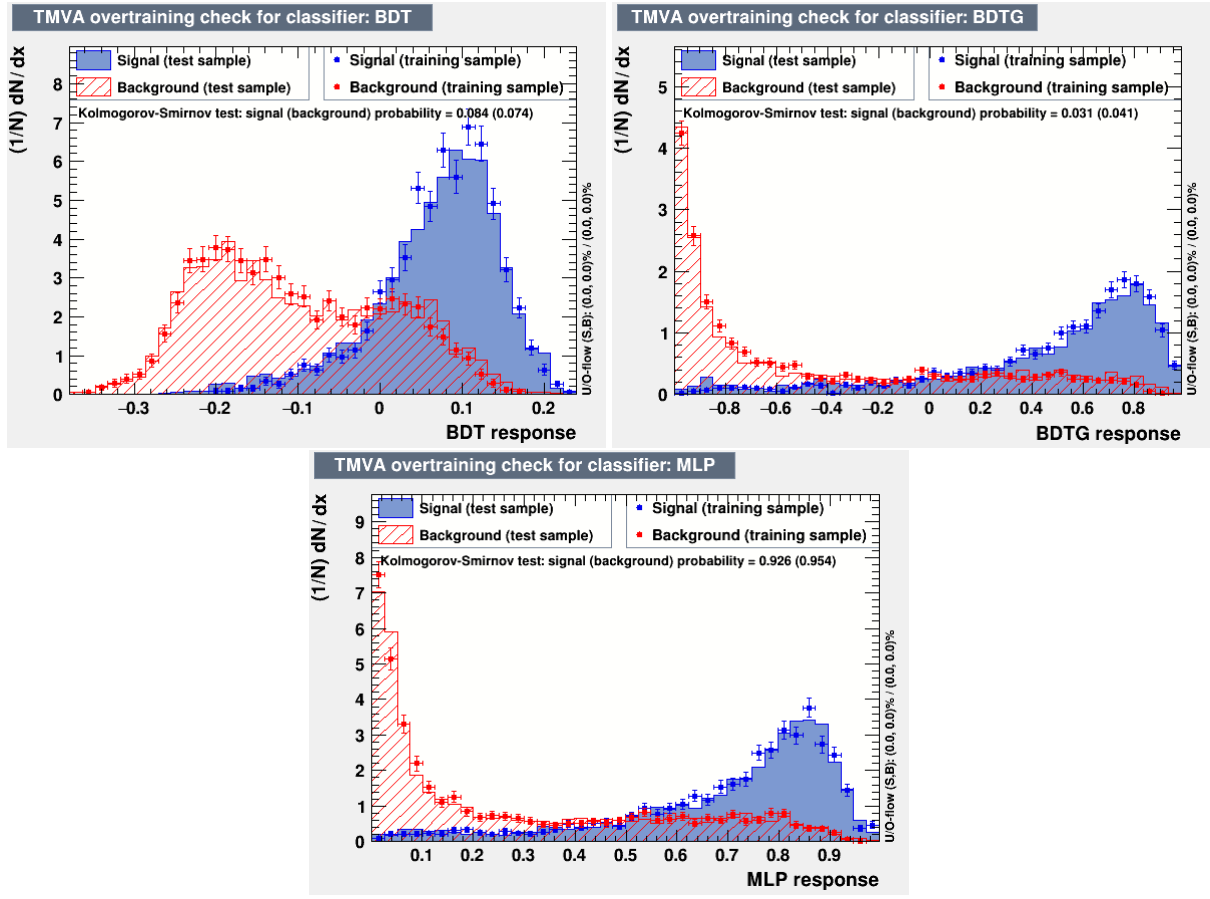


Figure 52: Response curves for MVA selectors: (top left) BDT, (top right) BDTG, (bottom) MLP. For each plot, the horizontal axis shows the MVA output and the vertical axis shows the normalised distribution. The output for the training sample is shown as points with error bars and the output for the test sample is shown as a shaded/hatched histogram.

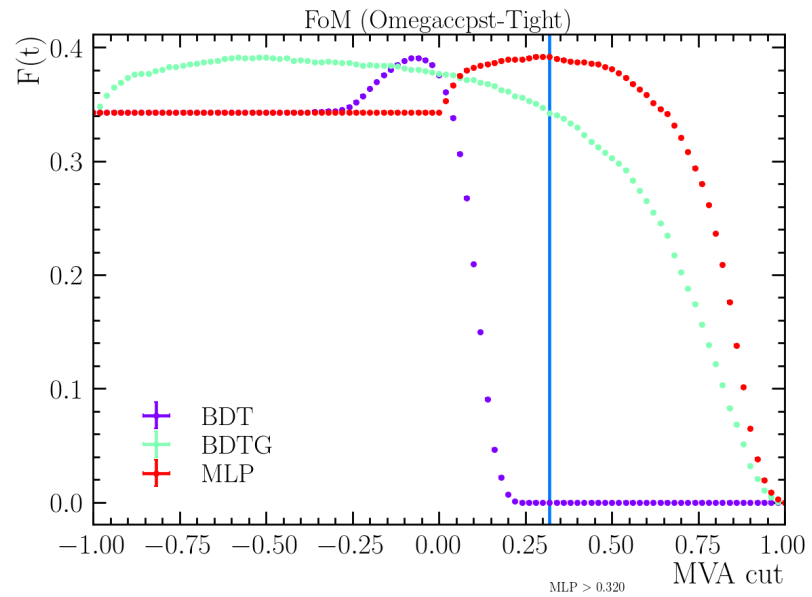


Figure 53: Dependence of the signal significance on the cut applied, for three different selectors.

References

- [1] M. Gell-Mann, A schematic model of baryons and mesons, Phys. Lett. **8** (1964) 214.
- [2] G. Zweig, An SU(3) model for strong interaction symmetry and its breaking, Part 1, 1964. CERN-TH-401.
- [3] G. Zweig, An SU(3) model for strong interaction symmetry and its breaking, Part 2, 1964. CERN-TH-412, Published in ‘Developments in the Quark Theory of Hadrons’. Volume 1. Edited by D. Lichtenberg and S. Rosen. Nonantum, Mass., Hadronic Press, 1980. pp. 22-101.
- [4] A. De Rujula, H. Georgi, and S. L. Glashow, Hadron masses in a gauge theory, Phys. Rev. **D12** (1975) 147.
- [5] Particle Data Group, R. L. Workman and Others, Review of Particle Physics, PTEP **2022** (2022) 083C01.
- [6] W. Roberts and M. Pervin, Heavy baryons in a quark model, Int. J. Mod. Phys. **A23** (2008) 2817, [arXiv:0711.2492](https://arxiv.org/abs/0711.2492).
- [7] D.-H. He et al., Evaluation of spectra of baryons containing two heavy quarks in bag model, Phys. Rev. **D70** (2004) 094004, [arXiv:hep-ph/0403301](https://arxiv.org/abs/hep-ph/0403301).
- [8] Z.-G. Wang, Analysis of the $\frac{1}{2}^+$ doubly heavy baryon states with QCD sum rules, Eur. Phys. J. **A45** (2010) 267, [arXiv:1001.4693](https://arxiv.org/abs/1001.4693).
- [9] C.-H. Chang, C.-F. Qiao, J.-X. Wang, and X.-G. Wu, Estimate of the hadronic production of the doubly charmed baryon Ξ_{cc} under GM-VFN scheme, Phys. Rev. **D73** (2006) 094022, [arXiv:hep-ph/0601032](https://arxiv.org/abs/hep-ph/0601032).
- [10] A. Valcarce, H. Garcilazo, and J. Vijande, Towards an understanding of heavy baryon spectroscopy, Eur. Phys. J. **A37** (2008) 217, [arXiv:0807.2973](https://arxiv.org/abs/0807.2973).
- [11] J.-R. Zhang and M.-Q. Huang, Doubly heavy baryons in QCD sum rules, Phys. Rev. **D78** (2008) 094007, [arXiv:0810.5396](https://arxiv.org/abs/0810.5396).
- [12] M. Karliner and J. L. Rosner, Baryons with two heavy quarks: Masses, production, decays, and decays, Phys. Rev. **D90** (2014) 094007, [arXiv:1408.5877](https://arxiv.org/abs/1408.5877).
- [13] LHCb collaboration, R. Aaij et al., Observation of the doubly charmed baryon Ξ_{cc}^{++} , Phys. Rev. Lett. **119** (2017) 112001, [arXiv:1707.01621](https://arxiv.org/abs/1707.01621).
- [14] LHCb collaboration, R. Aaij et al., Measurement of the lifetime of the doubly charmed baryon Ξ_{cc}^{++} , Phys. Rev. Lett. **121** (2018) 052002, [arXiv:1806.02744](https://arxiv.org/abs/1806.02744).
- [15] LHCb collaboration, R. Aaij et al., First observation of the doubly charmed baryon decay $\Xi_{cc}^{++} \rightarrow \Xi_{cc}^{+} \pi^+$, Phys. Rev. Lett. **121** (2018) 162002, [arXiv:1807.01919](https://arxiv.org/abs/1807.01919).
- [16] LHCb collaboration, R. Aaij et al., Precision measurement of the Ξ_{cc}^{++} mass, JHEP **02** (2020) 049, [arXiv:1911.08594](https://arxiv.org/abs/1911.08594).

- [17] LHCb collaboration, R. Aaij et al., Observation of the doubly charmed baryon decay $\Xi_{cc}^{++} \rightarrow \Xi_c^{\prime+} \pi^+$, JHEP **05** (2022) 038, [arXiv:2202.05648](https://arxiv.org/abs/2202.05648).
- [18] LHCb collaboration, R. Aaij et al., Search for the doubly charmed baryon Ξ_{cc}^+ , Sci. China Phys. Mech. Astron. **63** (2020) 221062, [arXiv:1909.12273](https://arxiv.org/abs/1909.12273).
- [19] SELEX collaboration, M. Mattson et al., First observation of the doubly charmed baryon Ξ_{cc}^+ , Phys. Rev. Lett. **89** (2002) 112001, [arXiv:hep-ex/0208014](https://arxiv.org/abs/hep-ex/0208014).
- [20] LHCb collaboration, R. Aaij et al., Search for the doubly charmed baryon Ξ_{cc}^+ , JHEP **12** (2013) 090, [arXiv:1310.2538](https://arxiv.org/abs/1310.2538).
- [21] LHCb collaboration, R. Aaij et al., Search for the doubly charmed baryon Ξ_{cc}^+ in the $\Xi_c^+\pi^-\pi^+$ final state, JHEP **12** (2021) 107, [arXiv:2109.07292](https://arxiv.org/abs/2109.07292).
- [22] LHCb collaboration, R. Aaij et al., Search for the doubly charmed baryon Ω_{cc}^+ , Sci. China Phys. Mech. Astron. **64** (2021) 101062, [arXiv:2105.06841](https://arxiv.org/abs/2105.06841).
- [23] A. V. Berezhnoy, I. N. Belov, and A. K. Likhoded, Production of excited states of doubly heavy baryons at the large hadron collider, Physics of Atomic Nuclei **83** (2020) 892.
- [24] T. Sjöstrand, S. Mrenna, and P. Skands, A brief introduction to PYTHIA 8.1, Comput. Phys. Commun. **178** (2008) 852, [arXiv:0710.3820](https://arxiv.org/abs/0710.3820); T. Sjöstrand, S. Mrenna, and P. Skands, PYTHIA 6.4 physics and manual, JHEP **05** (2006) 026, [arXiv:hep-ph/0603175](https://arxiv.org/abs/hep-ph/0603175).
- [25] I. Belyaev et al., Handling of the generation of primary events in Gauss, the LHCb simulation framework, J. Phys. Conf. Ser. **331** (2011) 032047.
- [26] C.-H. Chang, J.-X. Wang, and X.-G. Wu, GENXICC2.0: An upgraded version of the generator for computing cross sections and distributions, Comput. Phys. Commun. **181** (2010) 1144, [arXiv:0910.4462](https://arxiv.org/abs/0910.4462).
- [27] G. Cowan, K. Cranmer, E. Gross, and O. Vitells, Asymptotic formulae for likelihood-based tests of new physics, The European Physical Journal C **71** (2011) 1.
- [28] LHCb collaboration, A. A. Alves et al., The LHCb Detector at the LHC, JINST **3** (2008) S08005, Also published by CERN Geneva in 2010.
- [29] LHCb collaboration, LHCb detector performance, International Journal of Modern Physics A **30** (2015) 1530022.
- [30] LHCb collaboration, R. Aaij et al., Design and performance of the LHCb trigger and full real-time data processing, Journal of Instrumentation **14** (2019) P04013.
- [31] J. Albrecht, The LHCb Trigger System, Nuclear Physics B - Proceedings Supplements **187** (2009) 237, Proceedings of the 8th International Conference on Beauty, Charm and Hyperons in Hadronic Interactions.
- [32] A. Hoecker et al., TMVA: Toolkit for Multivariate Data Analysis, PoS **ACAT** (2007) 040, [arXiv:physics/0703039](https://arxiv.org/abs/physics/0703039).